COMPUTATIONAL MODELING OF ATOMISTIC DYNAMICS IN SEMICONDUCTORS AND MOLECULAR SENSORS

By

Keith Hyrum Warnick

Dissertation

Submitted to the Faculty of the

Graduate School of Vanderbilt University

in partial fulfillment of the requirements

for the degree of

DOCTOR OF PHILOSOPHY

in

Physics

December, 2013

Nashville, Tennessee

Approved:

Sokrates T. Pantelides, Ph.D

David E. Cliffel, Ph.D.

Richard F. Haglund, Ph.D.

Volker E. Oberacker, Ph.D.

Kalman Varga, Ph.D.

© Copyright by Keith Hyrum Warnick 2013
All Rights Reserved

ACKNOWLEDGEMENTS

This work was supported by Office of Naval Research (ONR) Multidisciplinary University Research Initiative (MURI) grant N-00014-08-1-0655, Defense Threat Reduction Agency (DTRA) grant HDTRA1-10-0047, and by the McMinn Endowment at Vanderbilt University. Calculations were performed on US Air Force Research Laboratory (AFRL), US Army Engineer Research and Development Center (ERDC) and Maui High Performance Computing Center (MHPCC) computing resources.

TABLE OF CONTENTS

Page

ACKNOWLEDGEMENTS iii

LIST OF FIGURES vi

Chapter

I. Density Functional Theory as a Probe of Matter 8

1.1. Introduction and background 8

1.2. Energy levels and optical spectra 12

1.3. Total energies 13

1.4. Nudged Elastic Band Method 13

II. Room-temperature Diffusive Phenomena in Semiconductors – The Case for AlGaN 18

2.1. Observed degradation in GaN/AlGaN HEMTs 18

2.2. Nudged elastic band method, strain and vacancies 25

2.3. Results – E-field activated charged vacancy migration 29

2.4. Implications for HEMTs and oxides 38

III. Room-temperature Reactions for Self-cleaning Molecular Nanosensors 40

3.1. Demand for molecular sensors 40

3.2. Tools for theoretical investigation 46

3.3. RT reaction activation of a two-step self-cleaning process 47

IV. Hydrogen Dynamics and Metallic Phase Stabilization in VO_2 57

4.1. VO_2 phase transition properties and device applications 57

4.2. Choice of tools for modeling and calculation 58

4.3. Phase stabilization and diffusive hydrogen transport 59

4.4. Implications for tuning of VO_2 properties and controlled hydrogen doping 64

Appendix

A. List of Refereeed Journal Articles 67

A.1. Work done as part of this thesis 67

A.2. Work done as an undergraduate 67

B. List of Talks and Posters at International Meetings 68

B.1. Talks done as part of this thesis 68

B.2. Talks done as an undergraduate 68

B.3. Posters done as part of this thesis 69

B.4. Posters done as an undergraduate 69

REFERENCES 70

LIST OF FIGURES

Figure Page

1.1: Schematic of the Nudged Elastic Band method for finding minimum energy paths and saddle points in the configuration space of a system....... 15

2.1: High resolution electron microscope (HREM) image of a groove and crack formed by degradation of the AlGaN layer under the drain-side gate edge. 19

2.2: Diagram of planar piezoelectric stress due to high electric field under the drain-side gate edge. 21

2.3: Diagram of trapping with drain-source voltage held at zero. G is the gate, S is source, and D is the drain. Gate current I_G and drain current I_D are labeled. Trap formation is indicated by the white lines and arrows. 22

2.4: AlGaN supercell.. 24

2.5: Vacancy formation energies in GaN and AlGaN as a function of Fermi level. 28

2.6: (a) The migration path of a Ga atom from a crystal site to a nearest vacancy site. (b) Isosurface of the negative (red) and positive (blue) difference in charge density between the perfect crystal and a triply negatively charged cation vacancy. 30

2.7: 2D device simulation of electric field profile of an AlGaN/GaN HEMT with the drain-source bias held at zero and a drain-gate bias of 40 V......... 33

2.8: (a) 2D simulated electric-field profile in an AlGaN HEMT with 40 V drain-gate bias. (b) Close-up of the superimposed pit................................ 35

2.9: Migration barrier of Al vacancy in AlGaN with cumulative barrier reductions due to mismatch strain, electric-field induced piezoelectric strain, and direct coulomb potential barrier lowering due to the electric field acting on the triply negatively charged vacancy. 36

3.1: Comparison of DNT (left) and TNT (right).. 43

3.2: Diagrams of (a) Fe-porphyrin and (b) 2,4-dinitrotoluene (DNT) molecules. 44

3.3: Initial (left) and final (right) states of the partial oxidation of the DNT methyl group by oxygen. 47

3.4: Top: profile of O_2 bound to the Fe center of Fe-porphyrin. Center: configuration of the adsorbed DNT on Fe-porphyrin. Bottom: simultaneous adsorption of O_2 and DNT. 49

3.5: Calculated energies of the first reaction with corresponding diagrams of the configuration changes. 51

3.6: Calculated energies of the second reaction with corresponding diagrams of the configuration changes. 52

3.7: Transition state configurations. 54

3.8: Calculated binding energies of O_2 and O on Mn-porphyrin, Fe-porphyrin, and Co-porphyrin. 55

4.1: Structural deformation of monoclinic VO_2 due to hydrogen doping compared to monoclinic and rutile VO_2. 60

4.2: Doping the monoclinic (M1) phase of VO_2 with one H for every four V atoms fills the band gap and produces a metallic state, similar to the rutile (R) phase. Removing the hydrogen from doped M1 VO_2 while fixing the other atoms still produces a metallic state through deformation alone. 61

4.3: Comparison of the density of states near the Fermi energy for H-doped monoclinic VO_2 and for the same fixed structure with all H atoms removed. Removing the hydrogen from doped M1 VO_2 while fixing the other atoms still produces a metallic state through deformation alone........ 62

4.4: A hydrogen interstitial bound to an oxygen in VO_2. Diffusion occurs primarily within the channel going into the figure. 63

4.5: A hydrogen molecule begins separated from the VO_2 (100) surface, then approaches the surface and splits towards adjacent oxygens with a 1.6 eV activation barrier, incorporating two atomic hydrogens into the VO_2 with a 0.2 eV net energy release. 66

CHAPTER I

DENSITY FUNCTIONAL THEORY AS A PROBE OF MATTER

1.1. Introduction and background

Modern computational theory of the physics of atoms and electrons began with the Schrödinger equation as formulated in 1925-1926 by Erwin Schrödinger.[1] This eigenvalue formulation encapsulates all information about a quantum mechanical system into a wave function. Observable properties are the expectation values of Hermitian operators with respect to that wave function. The basic form of the time-independent Schrödinger equation is

$$\hat{H}\psi(\boldsymbol{r}) = E\psi(\boldsymbol{r}) \tag{1.1}$$

where $\hat{H}$ is the Hamiltonian operator for the system, ψ is the wave function, E is the energy of the system, and r is a spatial coordinate vector. For a single particle in a fixed background potential V(r), this Hamiltonian takes the form

$$\left[-\frac{\hbar^2}{2m}\nabla^2 + V(\boldsymbol{r})\right]\psi(\boldsymbol{r}) = E\psi(\boldsymbol{r}) \tag{1.2}$$

This equation can be solved to obtain the energy levels and wave function of a single electron bound to a proton, i.e. a hydrogen atom. However, when additional electrons are added to the system, the resulting many-body system quickly becomes analytically unsolvable, as the potential each particle sees becomes

$$V(r) = \sum_{i=1}^{N}\sum_{j=i+1}^{N}\frac{Z_i Z_j}{|\boldsymbol{r}_i - \boldsymbol{r}_j|} \tag{1.3}$$

where i and j iterate over all particle-particle pairs, comprising electron-nucleus, nucleus-

nucleus, and electron-electron interactions, approximating all nuclei as point charges. The many-body problem can be greatly simplified by applying the Born-Oppenheimer approximation, which treats the locations of atomic nuclei as fixed and reduces their contribution to that of a static background potential. This allows the problem to be rewritten as

$$\left[\sum_{i}^{N}\left(-\frac{\hbar^2\nabla_i^2}{2m}+v(\mathbf{r}_i)\right)+\sum_{i<j}U(\mathbf{r}_i,\mathbf{r}_j)\right]\Psi(\mathbf{r}_1,\mathbf{r}_2\ldots,\mathbf{r}_N)=E\Psi(\mathbf{r}_1,\mathbf{r}_2\ldots,\mathbf{r}_N) \tag{1.4}$$

where $\sum_i^N v(r_i)$ is a background potential produced by the fixed nuclei to which the electrons respond, and $U(r_i,r_j)$ is the Coulomb interaction potential between any two electrons, given by

$$U(r_i,r_j)=\frac{1}{4\pi\varepsilon_0}\frac{e^2}{|\boldsymbol{r}_i-\boldsymbol{r}_j|} \tag{1.5}$$

This system is far simpler than the full many-body time-independent Schrödinger equation, but is still intractable without further approximations and insights. One of the more successful modern methods for finding useful approximate solutions of the full many-body Schrödinger equation is density functional theory.

Since the foundational work of Walter Kohn, Pierre Hohenberg, Lu Sham, and others, density functional theory (DFT) has become a well-developed and powerful tool in the theoretical study of condensed matter. DFT circumvents the intense difficulty of solving the many-body Schrödinger equation by use of the Hohenberg-Kohn (HK) theorem, which proves that the many-body wave function *uniquely* determines the ground-state electron density, *and vice versa*.[2] Thus it is not necessary to explicitly solve the many-body Schrödinger equation to obtain the information inherent in the full

ground-state wave function: any method that produces the ground-state density is equivalent to solving the full Schrödinger equation for the wave function and implies all the same information.

Finding the electron density distribution constituting the ground state of the system can then be approached by exploiting its nature as an energy minimum in the configuration space of the system. If a given wave function is the ground state wave function for the Hamiltonian of the system, any other wave function produces a higher energy. By the HK theorem, the same is true of the ground state electron density distribution. However, the fundamental difficulty of solving a many-body problem of interacting particles remains.

To reformulate the problem in a more tractable form, the informational completeness and uniqueness of the ground-state density is exploited by the Kohn-Sham equations, which define a fictitious non-interacting system that results in the same density distribution as the true many-body system of interacting particles.[3] The equations have the form:

$$\left[-\frac{\hbar^2\nabla^2}{2m} + v_s(\mathbf{r})\right]\phi_i(\mathbf{r}) = \epsilon_i\phi_i(\mathbf{r}) \tag{1.6}$$

$$v_s(\mathbf{r}) = v(\mathbf{r}) + v_H(\mathbf{r}) + v_{xc}(\mathbf{r}) \tag{1.7}$$

where φ_i is the non-interacting wave function for a single particle, v(r) is the background potential from the nuclei, v_H(r) is the Coloumb interaction between the particle and the electron density due to the other electrons, and v_{xc}(r) is the exchange-correlation (XC) potential arising from the Fermionic nature of the electrons, comprising both exchange

and correlation effects. This formulation is not itself an approximation, but rather an exact reformulation of the problem.

Solving this much more tractable non-interacting system is equivalent to solving the full interacting system. The cost paid for converting the interacting system into an equivalent non-interacting one lies in the exchange-correlation (XC) potential term, which cannot be determined exactly except in the case of some very simple systems that do not require DFT at all. Thus DFT is formally an exact theory, but approximations of the XC potential are necessary for its practical implementation. Two common classes of approximations for the XC energy are the local density approximations (LDA) and generalized gradient approximations (GGA). For basic LDA, the XC energy is given by

$$E_{xc}^{LDA} = \int d\boldsymbol{r}\rho(r)\varepsilon_{xc}(\rho) \tag{1.8}$$

where $\varepsilon_{xc}(\rho)$ is the single-particle exchange-correlation energy for uniform electron gas of density ρ, from which the local density approximation derives its name. The exchange portion of this can be determined analytically, but the correlation requires further approximations, resulting in a large variety of existing functionals. GGA functionals additionally depend on the local gradient of the density, and provide more computationally expensive but potentially more accurate results.[4,5] Starting from these concepts, a large number of more complicated or hybridized functionals have been developed to produce more accurate calculations for specialized systems or features of interest. One such functional is the Perdew, Burke and Ernzerhof (PBE) functional, a type of GGA approximation that improves upon the local spin density (LSD) approximation, which is itself an extension of LDA that accounts for spin.[6,7] A yet further derivation is the PBE0 functional, which hybridizes the PBE exchange-correlation functional to

become

$$E_{xc}^{PBE0} = E_c^{PBE} + (1-\alpha)E_x^{PBE} + \alpha E_x^{HF} \tag{1.9}$$

where E_c^{PBE} is the PBE correlation functional, E_x^{PBE} is the PBE exchange functional, E_x^{HF} is the Hartree-Fock exchange, and α is commonly set to 0.25.[8–10] This hybrid functional replaces a fraction α of the PBE exchange with the Hartree-Fock exchange while leaving the PBE correlation term intact.

1.2. Energy levels and optical spectra

As the ground-state density implies all the information of the ground-state wave function, the electronic ground-state energy levels can be determined. Because excited states are inherently not part of this solution, this does not allow accurate calculation of transition energies and optical spectra. However, a time-dependent generalization of the Hohenberg-Kohn theorem known as the Runge-Gross theorem shows that the time-dependent density uniquely determines the time-dependent wave function.[11] This extension of the HK theorem to time-dependent, non-ground-state systems is the basis of time-dependent density functional theory (TDDFT), which allows the calculation of excited states, and hence, transition energies and optical spectra.

One noted and long-standing limitation of DFT in determining energy levels is its tendency to underestimate the band gap of bulk semiconductors. This has led to the use, where needed, of more complex or hybridized exchange-correlation functionals that are better-suited for specific systems.

1.3. Total energies

DFT can be used to determine the characteristics and structure of atomic defects in crystalline materials, such as vacancies, interstitials, antisite defects, and impurities. Knowledge of the properties of these defects allows a study of the cause of various phenomena in bulk materials, such as the defects and mechanisms responsible for observed traps in semiconductor band gaps. A typical value for α is 0.25.

As DFT can calculate the electronic ground-state total energy of a reasonably arbitrary arrangement of atoms, the energy barriers associated with specific changes in atomic configuration can also be examined, such as the migration of an interstitial or vacancy point defect in a bulk crystal to an adjacent crystal lattice site. By providing a series of intermediate atomic arrangements that smoothly transform between the initial and final configurations and evaluating the total ground-state energy of each, a profile of the change in total energy through the given process is obtained. By examining nearby migration processes and iteratively minimizing the energy barrier, the path with the lowest barrier between the initial and final states may be found.

1.4. Nudged Elastic Band Method

One commonly used implementation for obtaining a good representation of the lowest-energy reaction path and energy barrier profile is Nudged Elastic Band (NEB).[12,13] An illustrative schematic of this approach is shown in Figure 1.1. From an initial ordered list of atomic configurations (referred to as images) that represent the migration path to be explored, DFT is used to calculate for each image the electronic ground-state energy and electron density distribution. The electron density distribution then allows the force exerted on each atom to be calculated. In addition to the force due to the electron density,

a virtual “elastic band” is added between equivalent atoms in adjacent images, applying another force proportional to and opposing their separation. To achieve the desired goal if finding the minimum energy path, only the component of the electronic forces perpendicular to the current reaction path and the virtual elastic band forces parallel to that path are applied. This makes numerical calculation of tangents to the reaction path a crucial part of the method’s implementation. Combining the forces due to the electron density and the virtual elastic bands, the atomic positions in each intermediate image are relaxed by moving the nuclei in the direction of and proportional to the total force. This is the “nudging” referred to in the name of the method. Because of the chain of elastic bands that exists for each atom as it transitions from the initial to the final state, the atoms in the intermediate images are prevented from simply relaxing to the low-energy initial and final states, and instead tend towards fairly even spacing along the low-energy path through the saddle point.

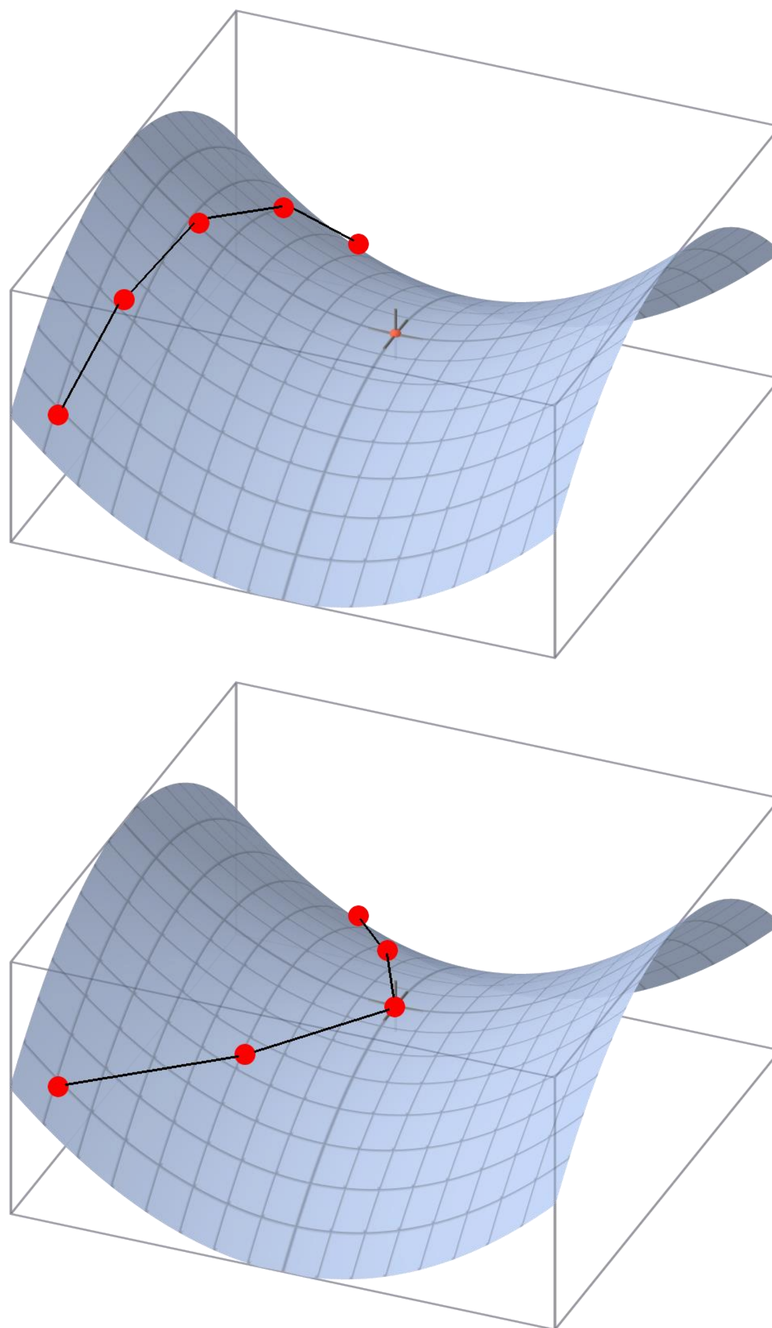

Figure 1.1: Schematic of the Nudged Elastic Band method for finding minimum energy paths and saddle points in the configuration space of a system. A series of configuration states (or "images") intermediate to a given initial and final state are created (top), and total energies and forces are calculated for each. A fictitious spring force is also added to keep the images spaced out along the reaction path. The images are then allowed to relax slightly under these total forces and descend the local energy landscape, and the process is repeated until convergence is reached (bottom). The minimum energy paths discovered this way represent the strongest probabilistic component of the associated hypothetical change in the atomic configuration of the system, and set the minimum activation barrier.

One refinement to this method is the Climbing Nudged Elastic Band (cNEB), where the highest-energy image is not subject to the elastic band forces from its adjacent images and the component of the electronic force along the reaction path is reversed and applied, causing the image to climb to the saddle point along the path.[12] When fully relaxed, this image represents the transition state. This method works best when the climbing image is close to the transition state, making it preferable to perform a regular NEB calculation first and apply cNEB to the result to refine the transition state. The transition state can be further verified by calculating the vibrational modes of the system, of which there should be only one that indicates instability in movement across the saddle point. Other classes of methods in computational chemistry for locating transition states and energies from DFT calculations are the synchronous transit, string, and dimer methods.

The energetics of defect reactions, such as the mutual annihilation of a vacancy and interstitial, two isolated vacancies joining into a divacancy, etc., can be analyzed in a fashion similar to point defect migration. The differences in total energy and charge distribution between the initial and final states, as well as the energetics of the intermediate states on the lowest-barrier path, can be found as long as the transition can be broken into a chain of sufficiently small shifts in atomic positions. More than one such chain of images may be necessary in transitions that incorporate a metastable state, for instance.

The ground-state structure of chemicals and structures adsorbed onto surfaces is important for surface reaction physics. The ability of DFT to be implemented in algorithms that iteratively relax atomic configurations to a stable low-energy state applies

equally well to adsorbates on a surface as it does to defects in bulk crystals.

The binding energy of an atom or molecule to another atomic system can be calculated by comparing the total energies of the joined set of atoms to the sum of the total energies of each part in isolation. The difference is the binding energy. This value is needed to determine the stability and reaction kinetics of molecules and structures.

CHAPTER II

ROOM-TEMPERATURE DIFFUSIVE PHENOMENA IN SEMICONDUCTORS – THE CASE FOR AlGaN

2.1 Observed degradation in GaN/AlGaN HEMTs

Diffusion in solids is a ubiquitous phenomenon driven by gradients of thermodynamic variables such as concentration, chemical potential, temperature, pressure, electrostatic potential (for charged species), etc. For electrons, the term diffusion is usually reserved for transport driven by concentration gradients, whereas transport driven by an electrostatic potential gradient is called drift. For atomic transport, interstitial atoms in crystals are often very fast diffusers even at room temperature (RT). Diffusion of substitutional impurities and host atoms (self-diffusion), on the other hand, is typically mediated by native point defects such as vacancies and interstitials. The diffusion coefficient depends exponentially on the activation energy, which is the sum of the formation and migration energies of the pertinent defect. In metals, vacancy formation and migration energies are typically small and self-diffusion phenomena are common at RT. In particular, electromigration, where self-diffusion is driven by electrical currents, is known to occur in metals, causing plastic deformation and voiding.[14,15] Metals are also known to undergo diffusive creep, also known as Nabarro-Herring creep, caused by self-diffusion driven by external stress. In bulk semiconductors, however, self-diffusion and substitutional-impurity diffusion are known to occur only at high temperatures.[16–19] In particular, in silicon, the migration energies of native defects in the bulk are small, but their formation energies are very large (>3 eV), resulting in prohibitively large activation energies. However, electromigration is possible on semiconductor surfaces, where

vacancies are naturally present.[20] In bulk compound semiconductors, vacancy formation energies are often small when the Fermi energy is near a band edge.[21–24] However, migration energies are large because vacancy migration entails an atomic hop to a second-neighbor site.

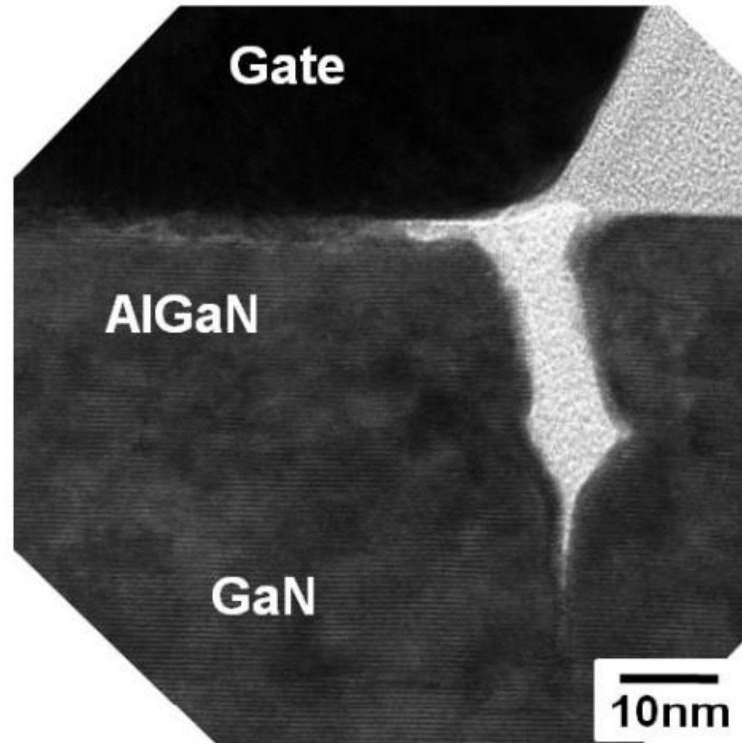

Figure 2.1: High resolution electron microscope (HREM) image of a groove and crack formed by degradation of the AlGaN layer under the drain-side gate edge. Adapted from Park et. al.[28]

Recent RT observations of plastic deformation in n-type AlGaN/GaN high-electron-mobility transistors (HEMTs) have been attributed to diffusive phenomena.[25–30] The primary evidence of physical degradation is TEM observation of the formation of grooves and pits in the surface of the AlGaN/GaN crystal under the drain-side edge of the gate, with the pits growing and merging to form deep groves, and eventually, cracks. Figure 2., adapted from Park et al., depicts an example device cross-section of an instance

of severe degration.[28] The deformation occurs in the absence of currents, ruling out electromigration via an "electron wind" effect, which can occur in metals.[14,15] Device simulations and experimental data also rule out self-heating and hot electron effects.[25] However, several classes of possible mechanisms have also been proposed and partially explored. In these AlGaN/GaN HEMT structures there exists an inherent strain in the AlGaN epilayer due to lattice mismatch, with additional strain induced by the electric field because of the inverse piezoelectric effect that results from the lack of crystallographic inversion symmetry in wurtzite GaN and AlGaN, as depicted in Figure 2.2, adapted from Joh and del Alamo.[29,31] Since degradation is also observed to be activated by an electric field above a critical value, this supports the possibility of a strain-based activation triggered through the additional piezoelectric strain. Relief of this net strain through the formation of crystal dislocations has been suggested as the primary driver of the observed deformation.[25] While dislocation formation does relieve strain, it has also been suggested that this cannot entirely account for the observed deformation progression from shallow grooves to deepening pits and cracking. Another possible mechanisms is carrier trapping leading to a current collapse that has been observed in GaN HEMTs, with traps occurring either inside the AlGaN layer or on the device surface, as shown in Figure 2.2, adapted from Joh and del Alamo.[31] By comparing device characteristics at different temperatures, both trapping processes that are and are not thermally activated have been determined to be present. As the critical voltage for degradation is reached, the number of traps increases and their spectrum broadens, and are cited as being consistent with trap formation through the inverse piezoelectric effect. In addition to the dislocation and trap formation mechanisms, there may also be thermally

activated diffusive processes in the presence of electric field mediating the observed deformation.[25,26,28,30] This is supported by the apparent positive correlation with temperature, which the dislocation formation mechanism does not predict. At higher ambient temperatures, degradation is faster and more extensive, though there is no significant self-heating. However, the mechanism or mechanisms that enable RT self-diffusion has not been positively identified. Degradation is observed to coincide with a region of very high electric field under the bias conditions that produce degradation. This applies both when bias conditions are such that a high field is under both gate edges or just one.

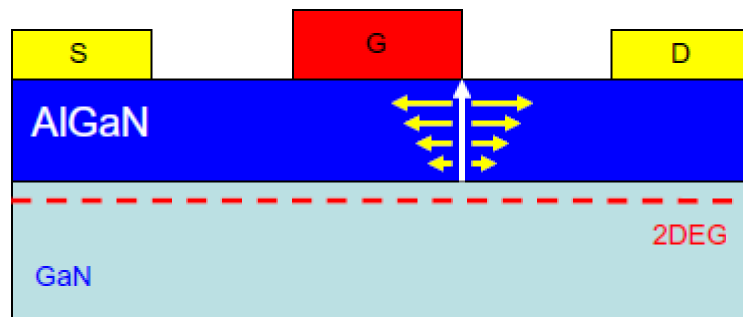

Figure 2.1: Diagram of planar piezoelectric stress due to high electric field under the drain-side gate edge. Adapted from Joh and del Alamo.[31]

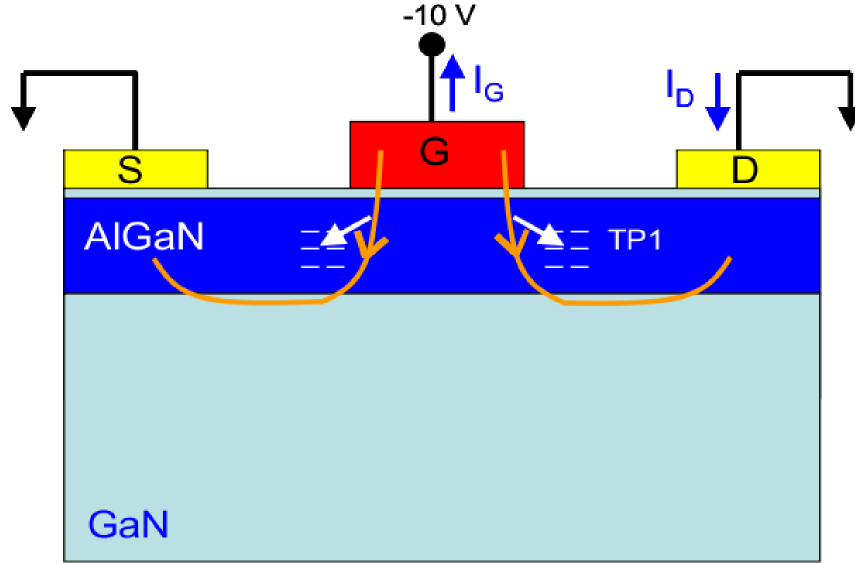

Figure 2.2: Diagram of trapping with drain-source voltage held at zero. G is the gate, S is source, and D is the drain. Gate current I_G and drain current I_D are labeled. Trap formation is indicated by the white lines and arrows. Adapted from Joh and del Alamo.[31]

In this chapter we report the results of first-principles density-functional calculations that allow us to identify the enablers of self-diffusion at RT in GaN/AlGaN structures and show that they are likely to occur in other semiconductors, especially oxides. We calculate formation and migration energies of vacancies under strain and electric fields. When the GaN substrate is n-type and the Fermi energy is near its conduction band edge, the formation energies of cation vacancies in unstrained AlGaN are near zero but their migration energies are too large, >1.5 eV, for appreciable diffusion at RT (typically the sum of formation and migration energies, i.e., the diffusion activation energy, must be ~1 eV or lower for diffusive processes to be appreciable at RT). We further find that application of strain, even at substantial levels, has little effect on either formation or migration energies. However, the pertinent cation vacancies are *triply negative*, whereby application of an electric field lowers the barrier for migration anti-parallel to the field by

a significant amount. At the observed critical values of the field, the net activation energy is reduced to approximately 1 eV, so thermally-activated atomic migration becomes appreciable at RT, driven by the electric field. These results provide a mechanism for plastic deformation mediated by vacancies, much like Nabarro-Herring creep and dislocation climb, but with an electric field being the main driver (vacancy drift). In addition to this process, the presence of unusually high local strain can also lead to dislocation glide and further formation of dislocations via strain relaxation, compounding the role of vacancy migration processes.[25,26,32,33] This anisotropic defect migration is expected to occur in any crystalline material in the presence of a high external electric field whenever low-formation-energy native point defects exist in a high-charge state, provided that the activation energies in the absence of external field are approximately 1.5 eV or less. To support a high external field, a large band gap is required. Oxygen vacancies in several oxides fit these criteria, including ZnO, TiO_2 and HfO_2.[34–36] Many transition-metal oxides, especially those doped with cations of lower oxidation state, have large O vacancy concentrations as processed, bypassing the requirement of low vacancy formation energies. One such example is Y-doped ZrO_2, in which a fraction of Zr^{+4} are replaced by Y^{+3}.[37]

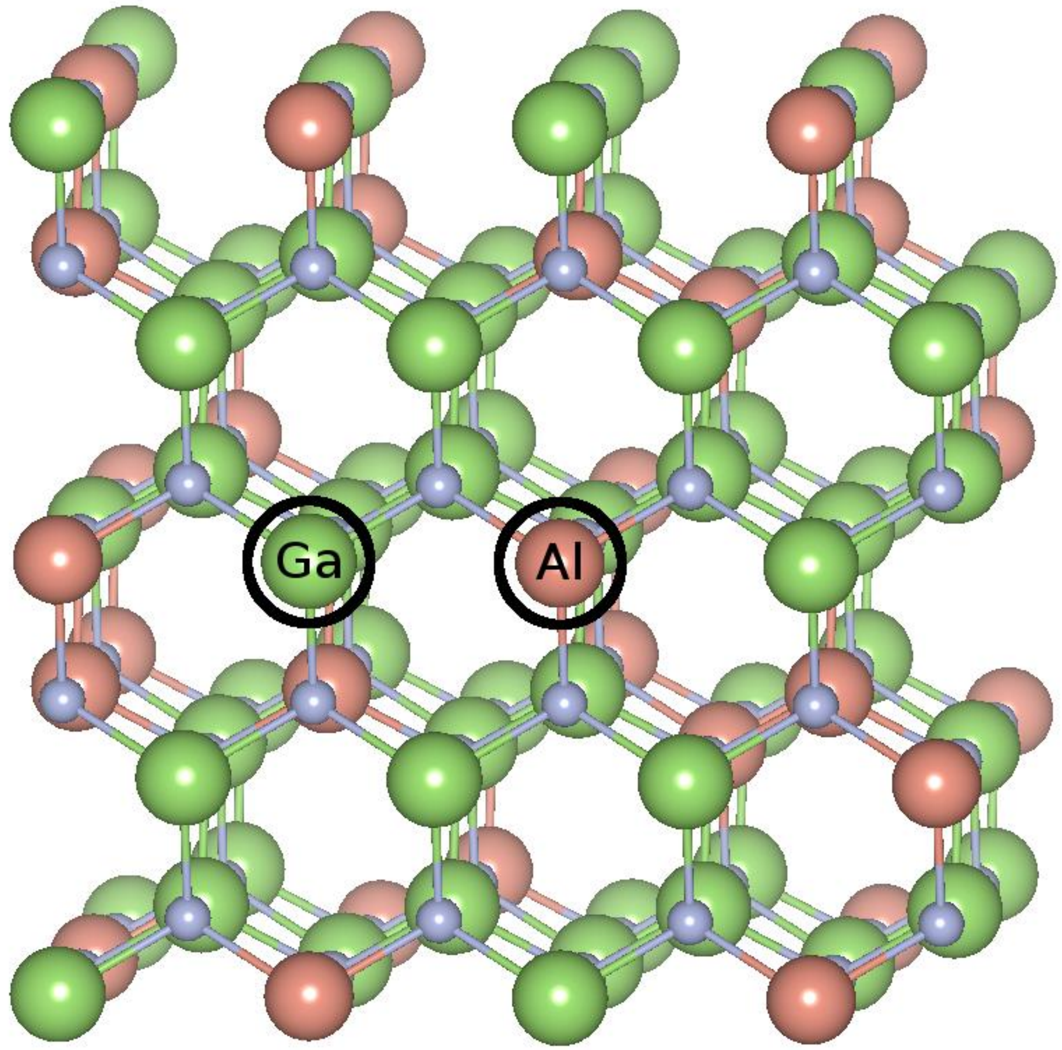

Figure 2.3: AlGaN supercell. Vacancies are formed by removing an atom of the complete supercell, such as the Ga and Al atoms circled.

2.2 Nudged elastic band method, strain and vacancies

We used density functional theory with the gradient-corrected local density approximation (GGA) as implemented in the VASP code.[5] Ultrasoft pseudopotentials were used to replace core electrons, wherein the core electrons are replaced with a pseudopotential that approximates their contribution to effects on ground-state electron density distribution.[38] Far fewer high-energy plane waves are required in the basis set to achieve convergence, and both memory and computational requirements are greatly decreased. Approximating the core electrons with a static potential in this manner is valid for low-energy configurations, as structural and chemical properties are overwhelmingly determined by valence electron behavior only. The plane wave basis energy cutoff was set at 300 eV. A single *k*-point at $2\pi/a(1/4,1/4,1/4)$ was employed for Brillouin zone integrations. We used supercells of 128 atoms in a wurtzite structure with periodic boundary conditions. Several configurations were used for the distribution of Al atoms in AlGaN; the results do not vary significantly. The difference in results between GaN and AlGaN comes primarily from the change in lattice constant. Atomic positions were relaxed until the configuration energy difference was less than 10^{-4} eV. Migration barriers were calculated using the nudged elastic band (NEB) method.[12,13]

For GaN, the relaxed lattice constant is a = 3.207 Å with c/a = 1.63. For AlGaN the relevant Al/Ga fraction is $Al_{0.3}Ga_{0.7}N$, with a relaxed lattice constant of a = 3.138 Å and c/a = 1.63.[26] The strongest source of strain on the thin AlGaN layer is lattice mismatch with the GaN substrate. The AlGaN layer are below the critical thickness for strain relaxation by misfit dislocations, and the planar strain from being forced to match the lattice constant of the bulk GaN substrate should be approximately constant throughout the layer. As such, lattice mismatch of the AlGaN epilayer on the GaN substrate is

reflected by expanding the AlGaN lattice constant to match that of GaN, resulting in a 2.2% planar expansion.[39,40]. By solving the corresponding special case of plane stress Hooke's law with experimentally determined elastic modulus and Poisson ratio this 2.2% expansion in the interface plane produces a 1.5% compression in the perpendicular direction; the AlGaN parameters under this strain are a' = 3.207 Å, c'/a' = 1.571. This approximate strain is expected to hold throughout the AlGaN epilayer since no relaxation through misfit dislocation formation is expected for thin (critical thickness ~50 nm) AlGaN layers.[39,40] The bulk GaN substrate is not similarly subject to lattice mismatch strain.

Two-dimensional numerical device simulations, using the Synopsys DESSIS simulator, were performed to obtain the electric field profile in representative HEMTs. The source and the drain voltages in these simulations were 0 V, with the gate at −40 V. The AlGaN barrier is 30 nm thick.

As shown previously in, the electric field in the AlGaN epilayer under the observed degradation conditions is approximately 10 MV/cm, which induces a ~3.5 GPa planar stress in both GaN and AlGaN through an inverse piezoelectric effect.[29,41,42] By Hooke's law, the corresponding strain is an approximately 1% axial compression and 0.25% planar expansion of both AlGaN and GaN lattices. For GaN the corresponding parameters for piezoelectric strain are a' = 3.215 Å with c'/a' = 1.61, and in AlGaN the parameters for the combination of lattice mismatch and piezoelectric strain are a' = 3.215 Å with c'/a' = 1.551.

Vacancy formation energies were calculated for several charge states of vacancies in GaN and AlGaN. This can be calculated by comparing the total system energies with or

without a vacancy present, and accounting for the displaced atom and electron by chemical potentials. Under this formulation, particles are exchanged with a theoretical bath of particles with a certain potential cost for each species. The electron bath is at the Fermi energy, and atoms have their chemical potential defined by exchange with a theoretical bulk crystal. Exchanging electrons with the Fermi energy means that the formation energy of charged vacancies depends directly on the Fermi level location. Atomic configurations used to calculate formation energies of cation vacancies are shown in Figure 2.3 with the relevant atom being removed and the cell subsequently relaxed fully. For the purpose of formation energy calculation it is not possible to construct finite supercells that represent Al and Ga vacancies and maintain identical Al/Ga ratios. Either the vacancy supercells differ in Al/Ga ratio, or their corresponding defect-free supercells differ. As a result, although Al and Ga vacancies in AlGaN are statistically identical, calculation of their formation energies using finite supercells is not. However, in the conditions of interest with Fermi energy near the conduction band edge, as is the case in the n-type material produced by the Ga-rich growing conditions relevant to these GaN HEMT devices, such calculated formation energies were found to be the same. This exercise corresponds to checking the sensitivity of the results to the precise Al/Ga ratio in the material.

The charge state of the vacancy can strongly influence the local electronic interactions and hence the defect structure and barrier energies, and must be included in the DFT calculation. Upon adding a charge to the supercell and relaxing the atomic structure, the final electron density can be examined and compared to the bulk defect-free crystal to

find where the extra charge reside in the crystal, and whether it is well-localized or distributed across the bulk.

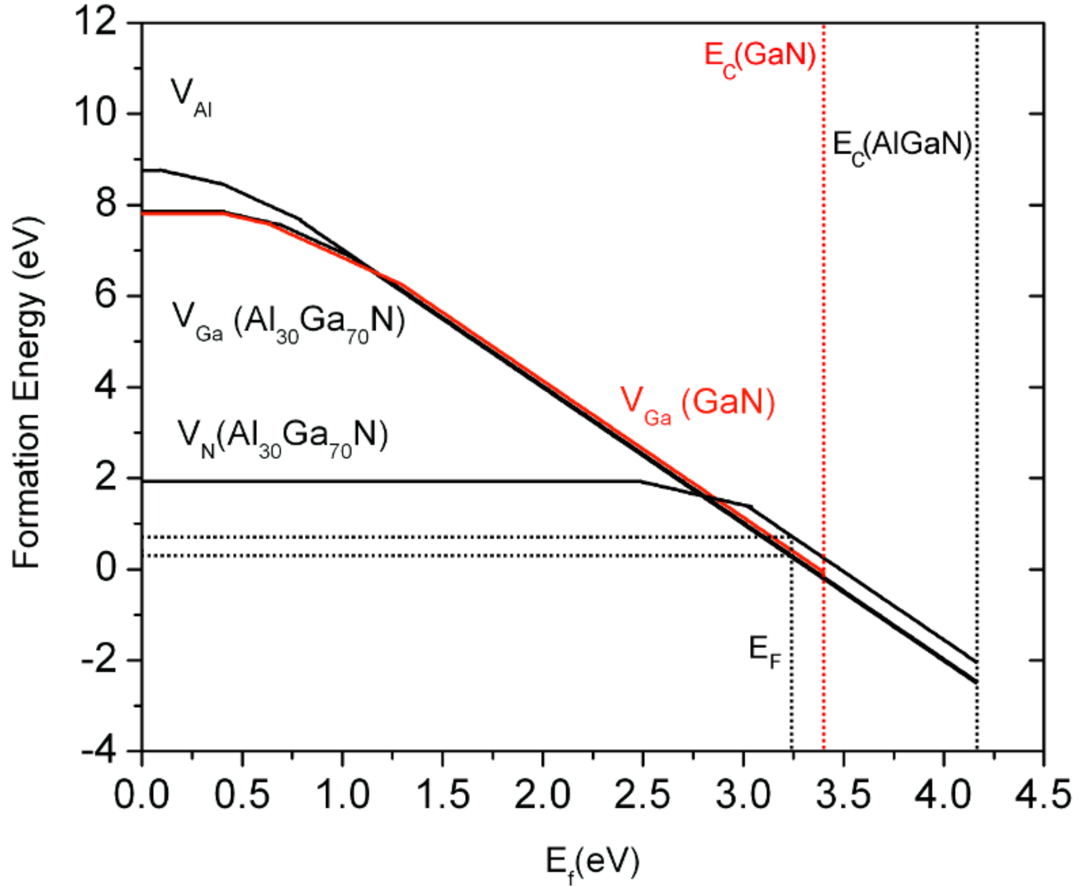

Figure 2.4: Vacancy formation energies in GaN and AlGaN as a function of Fermi level; slope indicates charge state. The expected Fermi level in the material and the associated formation energies are indicated by dotted lines, as are the conduction band edges in GaN and AlGaN. Due to differing stoichiometry and local environment, the calculated AlGaN cation vacancy formation energies differ at Fermi energies below 1 eV, though they are identical elsewhere

2.3 Results – E-field activated charged vacancy migration

Vacancy formation energies

Calculated vacancy formation energies in $Al_{0.3}Ga_{0.7}N$ and GaN under Ga-rich conditions are shown in Figure 2.4; these are consistent with previous work in GaN.[22–24,43,44] In n-type material, such as is the case for the Ga-rich growing conditions relevant to these GaN HEMT devices, we find that the triply-negative cation vacancy has the lowest formation energy, being effectively zero when the Fermi energy is at the GaN conduction band edge. Such a small formation energy suggests that cation vacancies especially should be plentiful in the bulk as-grown, though the vacancy concentration is unlikely to achieve its equilibrium value under typical growth conditions. The band gap of $Al_{0.3}Ga_{0.7}N$ is larger than that of GaN by about 0.8 eV, causing the formation energy of triply-negative cation vacancies to drop below zero when the Fermi energy is near the conduction-band edge.[45] Compensation by defects may, however, keep the Fermi energy from rising too close to the conduction band edge. Because the cation vacancy formation energies are near zero, the cation vacancy defect activation energies are approximately equal to the cation vacancy migration barrier energies. The calculated formation energy for N vacancies in GaN is approximately 0.5 eV higher than the Ga cation vacancy, and the formation energy of N vacancies in AlGaN is similar.

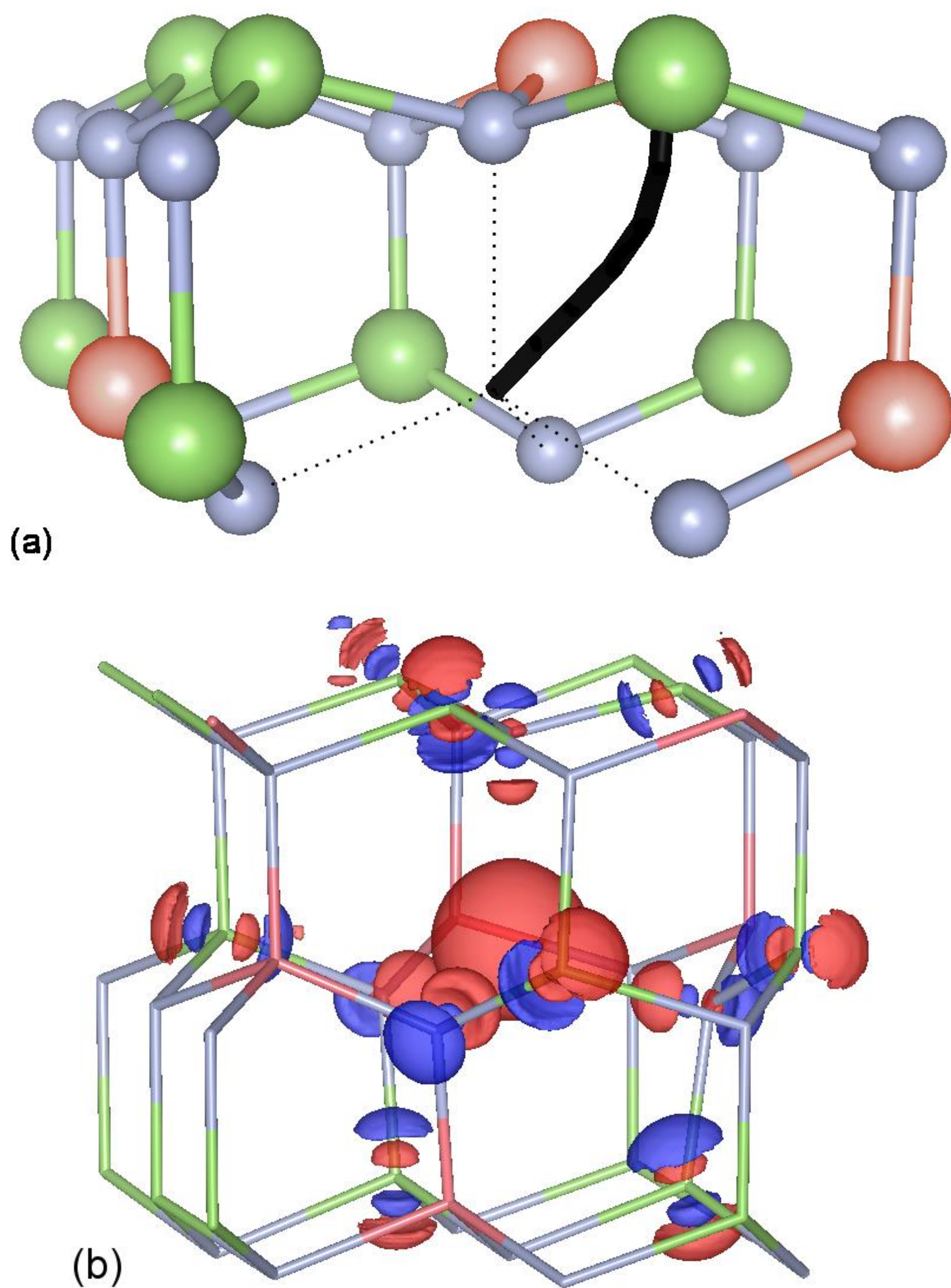

Figure 2.5: (a) The migration path of a Ga atom from a crystal site to a nearest vacancy site is indicated by the solid line. The dashed lines show the missing bonds prior to the migration. (b) Isosurface of the negative (red) and positive (blue) difference in charge density between the perfect crystal and a triply negatively charged cation vacancy. Atoms are not shown, but bonds are kept for reference.

Migration barriers

The calculated migration barrier for single Ga vacancies in unstrained GaN is 1.9 eV, and the N vacancy barrier is similarly 2 eV, in agreement with previous calculations.[22,23] In AlGaN the migration barrier for N vacancies is higher at ~2.2 eV. However, the migration barriers in AlGaN for Ga and Al vacancies are lower than their GaN counterparts at 1.8 eV and 1.6 eV, respectively. Figure 2.5(a) shows the path followed by a Ga atom in AlGaN during vacancy migration; this path is similar to those of other vacancies. Although cation vacancies are intrinsically identical, either an Al or Ga atom may move to produce vacancy migration, so they are distinguished as Al and Ga vacancy migration barriers. We have investigated migration paths parallel and perpendicular to the substrate; while planar stresses introduce further anisotropy to the crystal structure, we found the migration barriers to be isotropic, in agreement with previous work.[23]

After adding lattice mismatch strain to the AlGaN calculations, the resulting vacancy migration barriers are lowered for Ga and Al vacancies by 0.2 eV, becoming 1.6 and 1.4 eV, respectively. However, the migration barrier for N vacancies in AlGaN remains unaffected at 2.2 eV. We suggest that this occurs because Ga/Al atoms are relatively large, and are more sensitive to changes in the space around the migration path, while N atoms are smaller and less affected.

Adding piezoelectric strain to the lattice mismatch strain for the calculations for Ga and Al vacancies in AlGaN shows an additional barrier lowering of 0.1 eV, bringing their migration barriers to 1.5 and 1.3 eV, respectively. As before, N vacancy barriers are unaffected and remain at 2.2 eV. Ga and N vacancy migration barriers in GaN are also unaffected, remaining at 1.9 eV and 2 eV, respectively.

These migration barriers in both GaN and AlGaN are still too high to allow significant RT defect migration. However, the externally applied electric field acts on the triply negatively charged vacancy defects in n-type GaN and AlGaN and creates a potential bias for motion in the direction anti-parallel to the field, resulting in a significantly lower migration barrier in that direction. The local charge distribution associated with the triply negatively charged cation vacancy in shown in Figure 2.5(b). This charge distribution is obtained as the difference between total charge distributions of the perfect crystal and the charged vacancy. The charge is observed to be very well-localized to the site of the vacancy defect, supporting the presence of a Coulomb force acting on the localized charge resulting from the high local electric field. For localized charged point defects, we assume an approximately linear shift in charge distribution as the with respect to the atomic migration progress, and the resulting migration barrier lowering is given by

$$\Delta E_{migr} = Eqd \tag{2.1}$$

where E is the electric field strength along the direction of atomic migration, q is thecharge state of the defect, and d is the distance from the initial site to the point of highestenergy. Equation (1) assumes that any shift in charge distribution approximately corresponds to a simple translation, which produces an associated Coulomb potential difference. This is reasonable for the vacancy migrations in question because the field is approximately uniform over one migration step and the local charge density distribution relative to the vacancy site remains the same. As all the low-energy migration paths for single vacancies were found to consist of a single second-neighbor atom migrating to the vacancy site, the vacancy motion was represented as the reverse of the atom migration. Since the strength and sign of this barrier-lowering effect depend on the direction of

migration with respect to the external electric field, axial anisotropy is introduced to the vacancy diffusion.

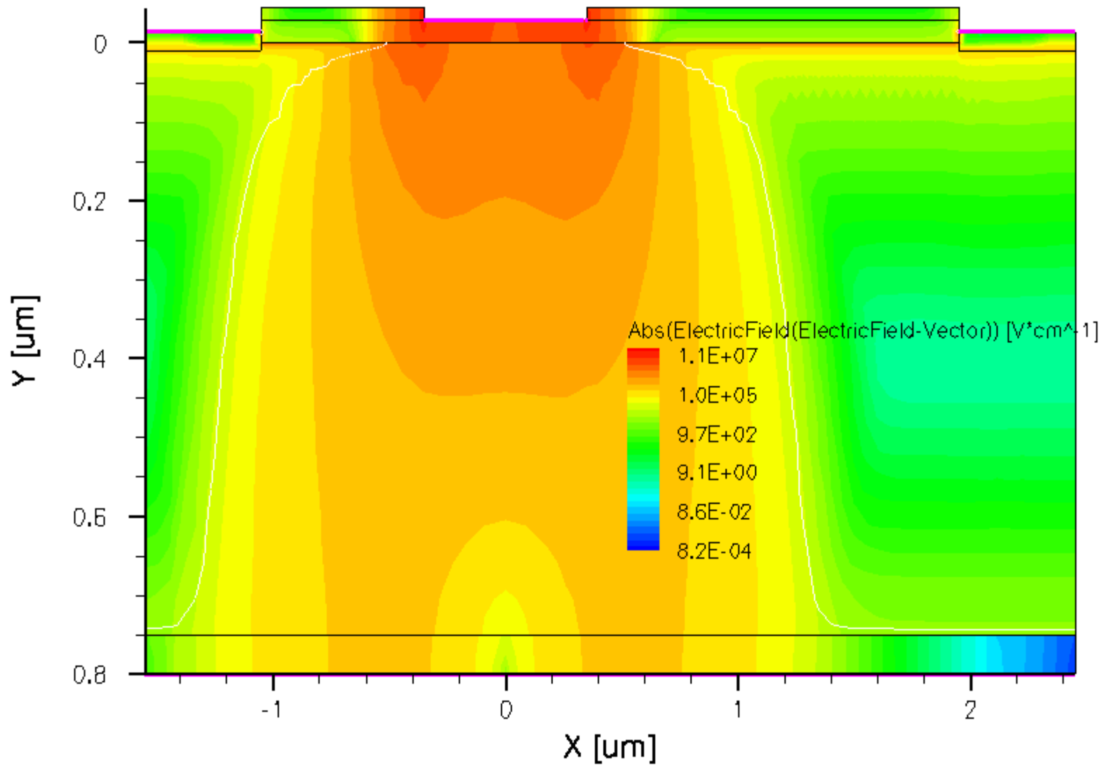

Figure 2.6: 2D device simulation of electric field profile of an AlGaN/GaN HEMT with the drain-source bias held at zero and a drain-gate bias of 40 V. Image courtesy of T. Roy. [46]

Figure 2.6, courtesy of T. Roy, shows a simulated electric field profile where the drain-source bias is zero and a gate bias of 40V produces a strong field.[46] A closer view of the region of interest with arrows showing the orientation of the field lines is given in Figure 2.7.[46] The peak electric field is E = 11 MV/cm, in agreement with previous calculations and observation.[41] The strong correlation between the location of the peak field and the location of physical degradation and mass transport strongly suggests that

electric field is a driving mechanism in the underlying degradation. Following Equation 1, with an external electric field of 11 MV/cm as exists in the peak under the gate, a vacancy charge of -3, and separation between adjacent (next-nearest neighbor) sites of ~3 Å, the energy reduction from a single hop anti-parallel to the field is 1 eV.[41] The barrier reduction is approximately` half of this, or 0.5 eV, as the peak of the minimum energy path would occur roughly halfway through the migration. This is a crude estimate however, and more exact results are made by applying Equation 1to every calculated point on the migration path, producing a lower peak energy that occurs earlier in the migration process. Doing this, the migration barriers of Ga and N vacancies in GaN after piezoelectric stress and electric field, noting that there is no mismatch strain in the GaN substrate, become 1.3 eV and 1.4 eV, respectively. The barrier for N vacancies in AlGaN after mismatch, piezoelectric, and electric field effects is 1.5 eV, too high for significant RT diffusion. However, the migration energies of Ga and Al vacancies in AlGaN under the combination of lattice mismatch, piezoelectric effect, and electric-field-induced barrier lowering become 1.0 and 0.9 eV, respectively. These values are sufficiently low to enable thermal migration of cation vacancies in AlGaN at RT. Figure 2.8 shows the migration barrier for an Al vacancy in AlGaN, which is qualitatively similar to the barriers for the other vacancies.

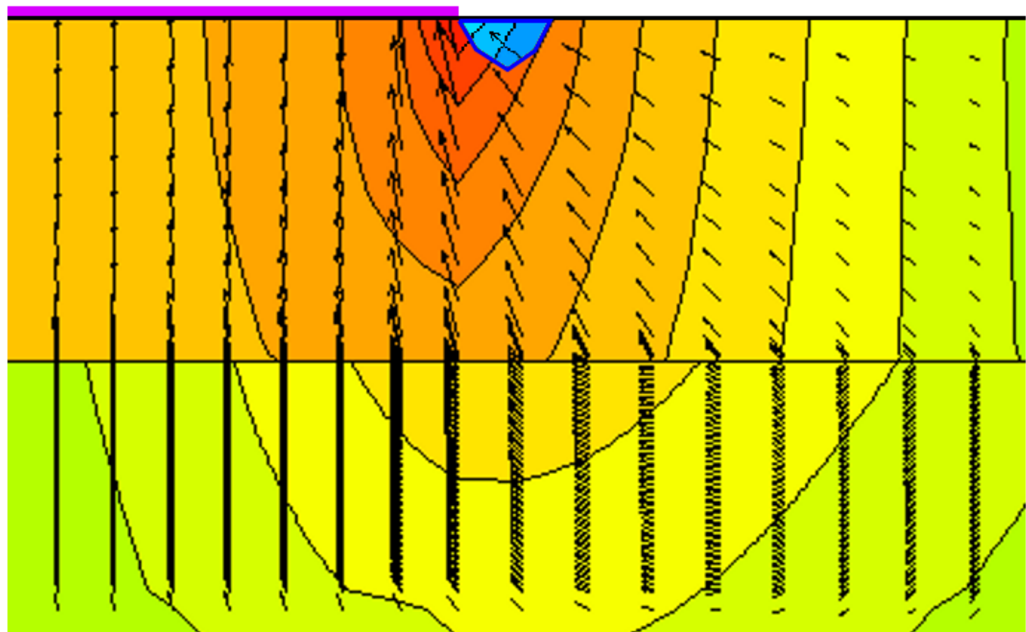

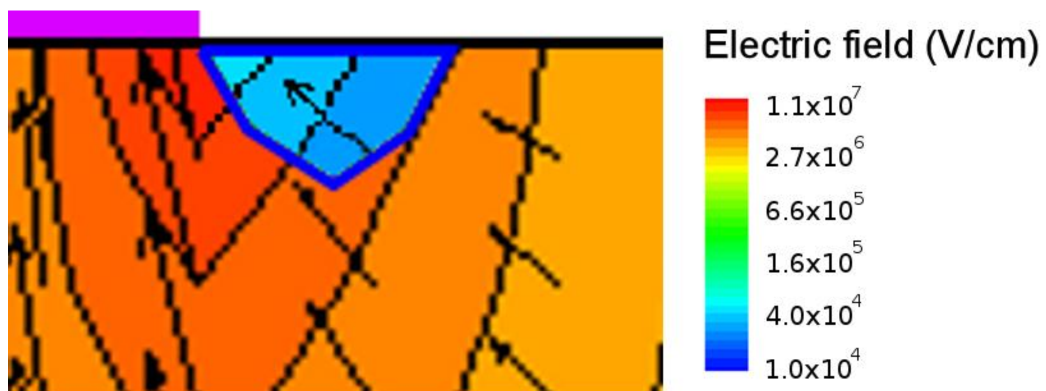

Figure 2.7: (a) 2D simulated electric-field profile in an AlGaN HEMT with 40 V drain-gate bias. The region near the drain-side gate edge is shown, with the gate depicted by the purple line. The top layer is AlGaN and the lower layer is bulk GaN. A typical early-degradation pit is superimposed in light blue. Arrows indicate E-field direction. (b) Close-up of the superimposed pit.

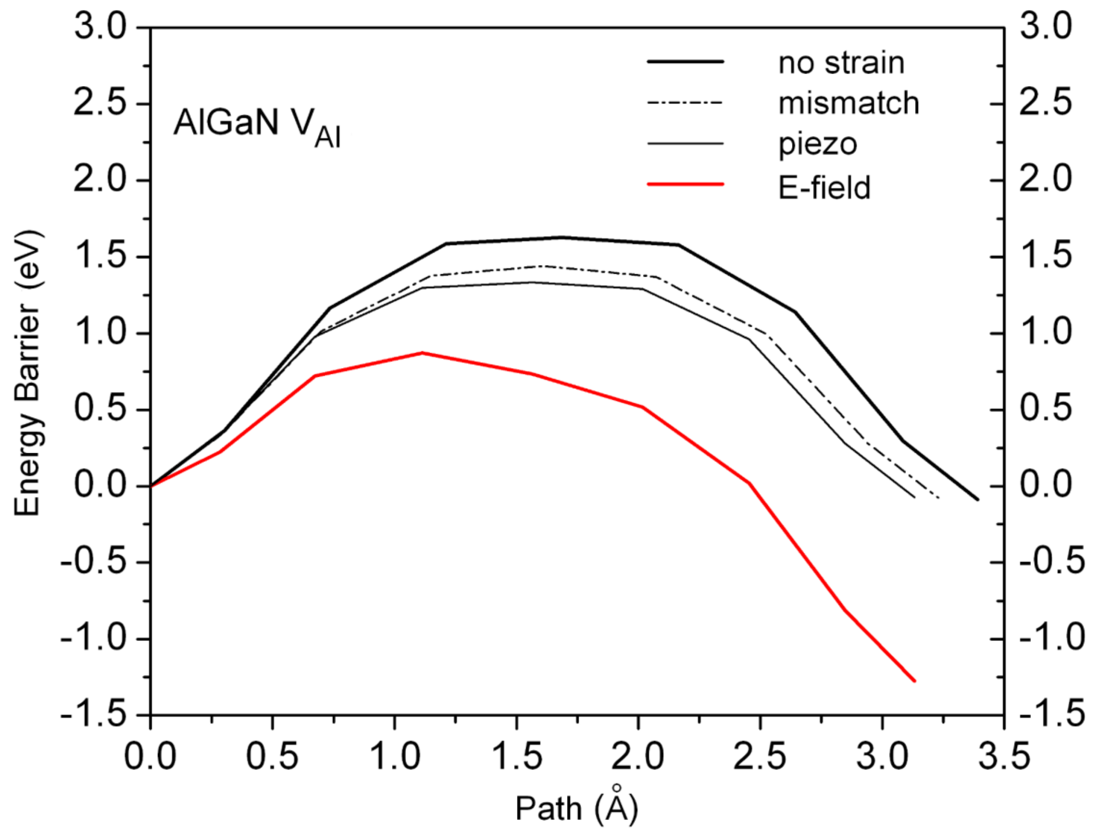

Figure 2.8: Migration barrier of Al vacancy in AlGaN with cumulative barrier reductions due to mismatch strain, electric-field induced piezoelectric strain, and direct coulomb potential barrier lowering due to the electric field acting on the triply negatively charged vacancy.

Diffusivity

The change in migration barrier is linear with respect to the electric field strength, while diffusion rates increase exponentially as barriers decrease. Thus, vacancies are mobile only in regions of sufficient electric field strength. The diffusivity is of the form

$$D = D_0 e^{-E_A/kT} \tag{2.2}$$

where k is the Boltzmann constant, T is the absolute temperature, and E_A is the activation energy for diffusion. Because of this, a reduction in activation energy from ~1.5 eV to 1 eV or lower represents a large increase in the expected diffusion rates. In addition, this mechanism for energy barrier lowering explains the temperature dependence, as higher thermal energies will produce even greater rates of diffusion. It also contributes to the understanding of the mass transport processes at work in this case, in accordance with earlier suggestions of diffusive mass transport.[30] With $E_A = 0.9$ eV, the exponent at RT is calculated to be −35.6. For comparison, in Devine et al. significant diffusion of oxygen vacancies has been reported with $E_A = 4.7$ eV at 1320 °C, which yields a nearly identical exponent of −34.2.[47] We conclude that significant vacancy diffusion is possible in AlGaN, with the important difference that migration is limited to the region of high electric field and is driven by a gradient in electric potential rather than chemical potential. The vacancies would concentrate near the edge of the high field region due to their biased migration, producing some locally trapped charge in the AlGaN layer. As seen in Figure 2.7, the size of the region where electric field is near 10 MV/cm is of order 10 nm, which agrees with the observed deformation.[26,30]

2.4 Implications for HEMTs and oxides

We conclude that triply-negative Al and Ga vacancies are mobile at RT in AlGaN in the presence of a high electric field. This thermally-activated diffusion of *triply-charged* vacancies through the bulk crystal lattice is similar to Nabarro-Herring creep, but with an electric field being the driver instead of inhomogeneous stress, producing a net migration of vacancies in the direction anti-parallel to the field.[16,17] The mobile Al and Ga vacancies can also induce dislocation climb, a mechanism whereby an edge or screw dislocation propagates by mobile vacancies merging into the dislocation, causing the defect edge to recede in what is known as negative climb.[32] The inverse process, when the edge emits vacancies and extends further through the lattice, is positive climb. Dislocation glide occurs in the presence of a local shear strain in the lattice cause the dislocation to travel through the lattice perpendicular to the edge.[32,33]Because there is a local strain due to lattice mismatch and the inverse piezoelectric effect, dislocation glide, dislocation generation, and possibly crack formation are also likely to be facilitated. The role of vacancy migration processes is therefore compounded, with plastic deformation being the inevitable outcome, as observed. However, the detailed nature of the processes that produce the observed deformation and ultimately device failure cannot be further elucidated at this time.

The RT plastic deformation reported by Joh and del Alamo et al. was attributed to diffusive processes, likely to be caused by a critical strain produced by lattice mismatch and a critical electric field.[25,26,28–30] Our theoretical results and analysis demonstrates that the origin of diffusive processes at RT is a combination of near-zero formation energies of triply-charged cation vacancies and a concomitant lowering of their migration energy by the electric field. An observable effect occurs when the activation energy is smaller

than ~1 eV, which makes diffusion observable at RT. As noted in the introduction, ZnO, TiO_2, HfO_2 and Y-doped ZrO_2 are candidate oxides for exhibiting this effect.[34–37] Similar RT diffusive processes should be significant for other materials with large band gaps (to support a high electric field), which also contain highly charged vacancies with activation energies of approximately 1.5 eV or less.

CHAPTER III

ROOM-TEMPERATURE REACTIONS FOR SELF-CLEANING MOLECULAR NANOSENSORS

3.1 Demand for molecular sensors

Demand for new molecular sensing techniques has come from a variety of pressing problems, such as detecting and disposing of explosive compounds and hazardous materials. Various molecular detection methods have gained prominence, including nanostructures that exhibit a change in fluorescence,[48–51] electronic resistance,[52,53] or other optoelectronic characteristics[54–57] when a target molecules is adsorbed. Typically, a refreshing step is required to return the sensor to its original state. The sensor can be refreshed by thermal desorption at elevated temperature, exposure to UV light, or application of chemicals.[50,53,55] Some sensor types cannot be refreshed at all and require chemical recycling to produce a new sensor.[49] Difficulty in refreshing these sensors limits their practical application.

DTRA grant HDTRA1-10-0047 motivated my research to shift from defect migration in bulk crystals to small molecule catalysis. This grant project aimed to produce basic research supporting the design of high-sensitivity autocatalytic self-cleaning chemical sensors without the use of reagents or active power. The proposed mechanism for this sensor relies on creating nanostructured surfaces that will autocatalytically react with adsorbed target molecules. The adsorption of these molecules creates a spectral shift in the surface plasmon resonance (SPR) of the substrate that can be detected optically, but this shift in the spectral peak of the extinction profile is typically nanometers or less, limiting sensitivity. To enhance this peak shift the autocatalytic nanostructure is placed

on a VO_2 substrate. Bulk VO_2 undergoes a semiconductor-to-metal transition at around 68° C, but this critical temperature can be reduced by either by doping bulk VO_2 or by selecting the size of VO_2 nanoparticles. By designing for a critical temperature near the operating temperature, the transition can be triggered by the adsorption and catalytic reactions of the adsorbed target molecules as they release enthalpic heat into the substrate. The electronic phase transition in the underlying VO_2 boosts the SPR shift in the surface nanostructure into the tens of nanometers range, making the sensor more sensitive and accurate. The main remaining factor in this scheme is a mechanism for enhancing selectivity. The proposal is to accomplish this by developing molecular recognition elements that will specifically bind to and facilitate the catalysis of target analytes while diminishing the access of non-target molecules to the catalytic sites. Recognition element strategies to be explored for this application will include peptide chains that are shown to have selective binding to various key targets such as DNT and TNT, and porphyrin cages. My component of this project has focused on identifying and characterizing catalysts and reactions that release heat from target molecules.

In this chapter we describe an approach to this alternative strategy for molecular sensing using a nanostructured substrate as a catalyst for a reaction between the target molecule and atmospheric oxygen. The energy released by the reaction is then absorbed by the substrate to produce detectable thermally-driven effects, such as the insulator-metal phase transition in VO_2, which can then be detected optically.[58] In particular, we report first-principles calculations for detection of 2,4-dinitrotoluene (DNT) molecules using Fe-porphyrin molecules as the active catalyst. The reaction begins as an O_2 molecule is adsorbed at the Fe site. Next, a hydrogen atom from the methyl group of

DNT is transferred to the bound O_2, followed by OH returning to DNT, releasing 1.9 eV per reaction. The residual bound oxygen atom can easily be removed by a second DNT molecule so that the process is self-cleaning with a further energy gain of 0.4 eV. All activation barriers are smaller than 1 eV (23 kcal mol^{-1}), which makes the process operable at RT. We estimate that the energy gain from DNT reactions can increase the temperature of a VO_2 nanoisland by 2°C, which can effectively trigger a phase transition of the VO_2 nanoisland near its critical temperature.

2,4,-dinitrotoluene (DNT) was chosen for initial study as a target reactant both because of its chemical similarity to the common explosive compound 2,4,6-trinitrotoluene (TNT), and because it is a precursor to other major industrial chemicals such as toluene diisocyanate (TDI), which is used in producing polyurethane plastics. DNT and TNT, comparatively depicted in Figure 3.1, are known to have very similar chemical properties, which might be expected as the only difference between them is that DNT has two NO_2 groups attached to the central six-carbon ring while TNT has three. However, DNT is useful as a proxy for TNT because it is easier and safer to work with in experiment. Besides TNT and its precursor DNT, toluene compounds in general are broadly used in industry and present challenges for production, management, and disposal.[59–61] In addition, various environment cleanup methods rely on oxidizing these compounds.[62–69]

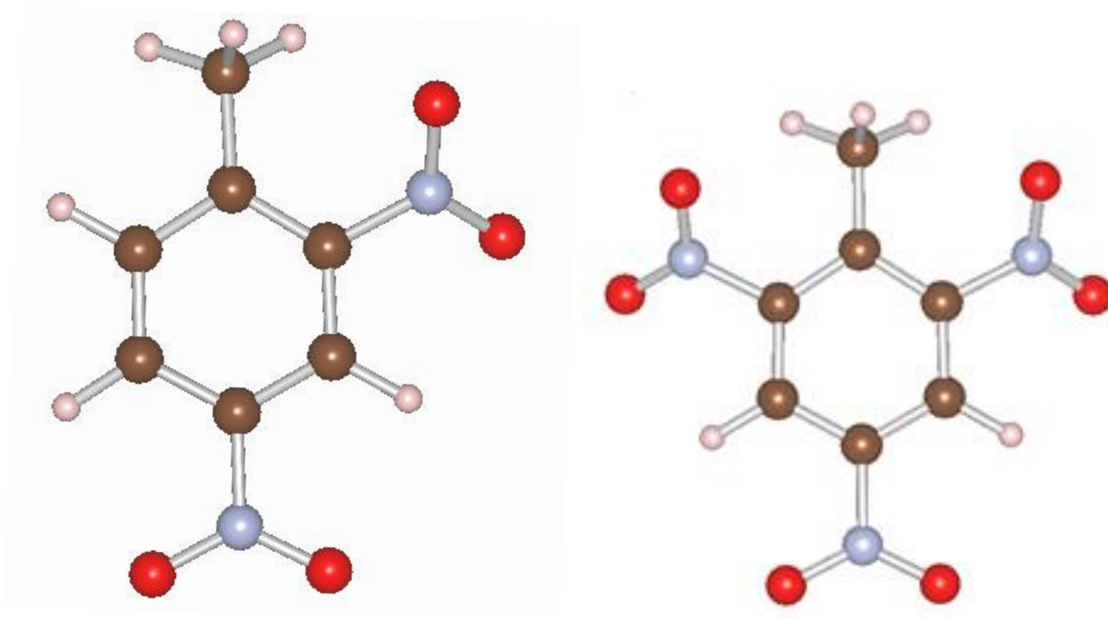

Figure 3.1: Comparison of DNT (left) and TNT (right). C atoms are brown, N atoms blue, O atoms red, and H atoms pink.

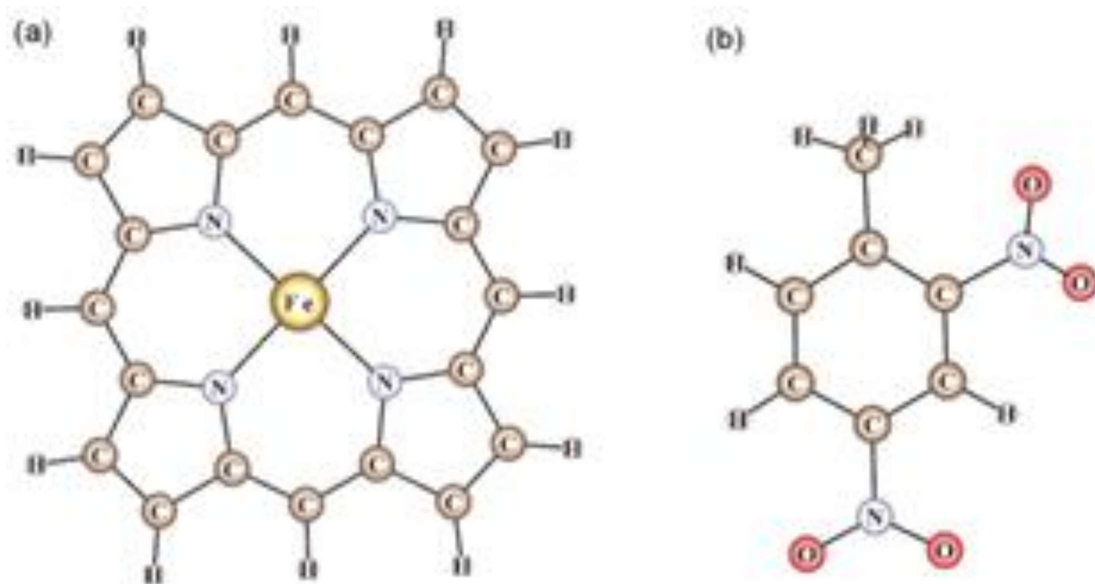

Figure 3.2: Diagrams of (a) Fe-porphyrin and (b) 2,4-dinitrotoluene (DNT) molecules.

As part of the focus on using autocatalysis in a detection scheme for explosives and other chemicals, a candidate catalyst must be selected for study. As these reactions will be occurring in normal atmosphere near room temperature, catalyzing reactions with atmospheric oxygen would be especially convenient. One possible candidate to meet these criteria is Fe-porphyrin, shown in comparison to DNT in Figure 3.2. Fe-porphyrin is one of various metalloporphyrins, a class of molecules that have proven valuable for catalyzing reactions in small organic molecules[70–73] and for non-catalytic molecular sensing.[74,75] Fe-porphyrin is well-known in biology as the center of the heme cofactor in hemoglobin. Though hemoglobin primarily binds and releases molecular oxygen for transport in blood, other heme proteins, such as heme peroxidases,[76,77] cytochrome-c oxidase,[78–80] and cytochrome P450 enzymes,[81–86] use Fe-porphyrin for catalyzing reactions that involve breaking O-O bonds. This ability to break O-O bonds makes Fe-porphyrin a prime candidate for catalyzing the oxidation of toluene compounds.

In order for the catalytic reaction to be userful for room-temperature detection by depositing energy into a substrate, it must be both catalytically activated at room temperature and sufficiently exothermic to make the released energy detectable. A catalyzed energy barrier of 1 eV or lower is required if there is to be a significant chance of the reaction occurring at room temperature. Similarly, the more exothermic the reaction is, the lower the reaction rate density on the substrate that is required for detection.

3.2 Tools for theoretical investigation

We used density functional theory as implemented in the VASP code with a plane-wave basis to perform binding energy and reaction pathway calculations.[5] Calculations were performed using the generalized gradient approximation (GGA) with the Perdew, Burke and Ernzerhof (PBE) functional for exchange and correlation.[6,7] The method of projector augmented wave (PAW) potentials[87] was used with a cutoff of 400 eV. Spin polarization was included in all calculations. All calculations were performed using a free Fe-porphyrin molecule, simulating a configuration where the porphyrin molecule is bonded to the substrate by peripheral ligands. The molecules were placed in a rectangular supercell with dimensions of 27×26×25 Å, large enough to isolate the reaction from being distorted by neighboring molecules that result from the periodic boundary conditions. A single k-point at the Γ point was used for Brillouin zone integrations. Reaction paths were calculated with the Climbing Nudged Elastic Band method.[12] Transition states were positively identified by calculating the associated molecular vibration modes, checking that there was only one significant imaginary vibrational mode, and further verifying that the mode corresponds to the expected shift in atomic configuration. All stationary states were converged until all atomic forces were less than 0.01 eV/Å.

3.3 RT reaction activation of a two-step self-cleaning process

DNT and TNT are known to be acceptably stable at room temperature in the presence of oxygen. To validate this known experimental result and establish a reference point for comparison with catalyzed reactions, we begin by performing calculations in the absence of the Fe-porphyrin catalyst. One oxygen reaction mechanism of interest consists of breaking an O_2 molecule and inserting one of the O atoms into the NH_3 group. The initial and final states of this reaction are depicted in Figure 3.3. Not depicted are the initial O_2 and remaining O reactant molecules.

By a NEB calculation, the barrier for this reaction is found to be far too high to occur at room temperature, chiefly due to the high binding energy of the O_2 molecule. The necessity of leaving one unbound O atom in the final state negates any energy released by this reaction, resulting in a 1.2 eV cost in transitioning from the initial to the final state. A catalyst is required for any such reaction to be feasible at RT.

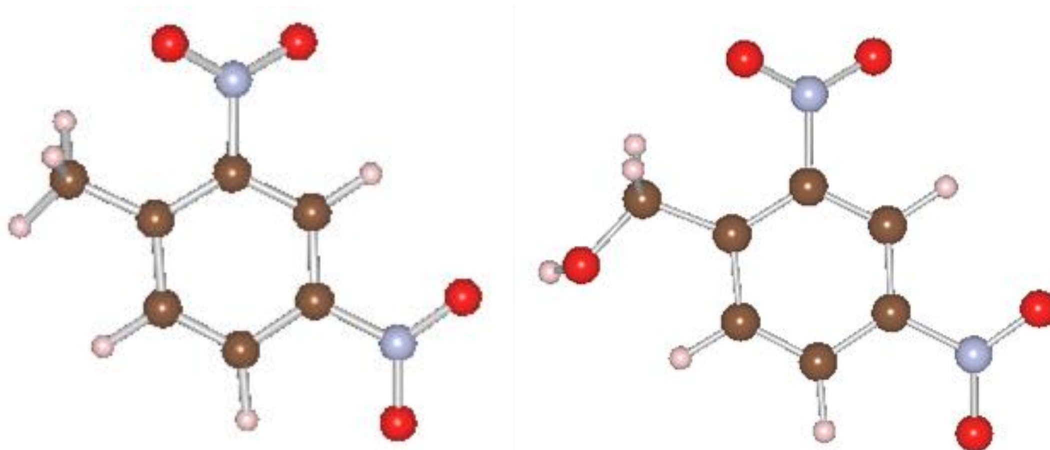

Figure 3.3: Initial (left) and final (right) states of the partial oxidation of the DNT methyl group by oxygen.

Adding the Fe-porphyrin catalyst introduces new influences on the target DNT and O_2 molecules that need to be assessed before considering the effect of the catalyst on the proposed partial oxidation reaction. By comparing total-energy differences between the Fe-porphyrin and either an adsorbed DNT or O_2 molecule allows the binding energies to be estimated at 1 eV and 2.6 eV for DNT and O_2 molecules, respectively. The various binding configurations in question are shown in Figure 3.4. When both molecules are adsorbed simultaneously, they must share the influence of the Fe center, causing binding energies to drop to 0.4 eV and 2.1 eV for DNT and O_2. The relatively strong binding of the O_2 by the Fe center contributes to a weakening of the O-O bond, which contributes to lowering the reaction barrier. In addition, the O_2 is strongly bound at room temperature, while the DNT molecules will occasionally attach and detach from the Fe center due to their relatively low binding energy. Note that the relaxed configuration calculated brings the desired reaction centers into close proximity.

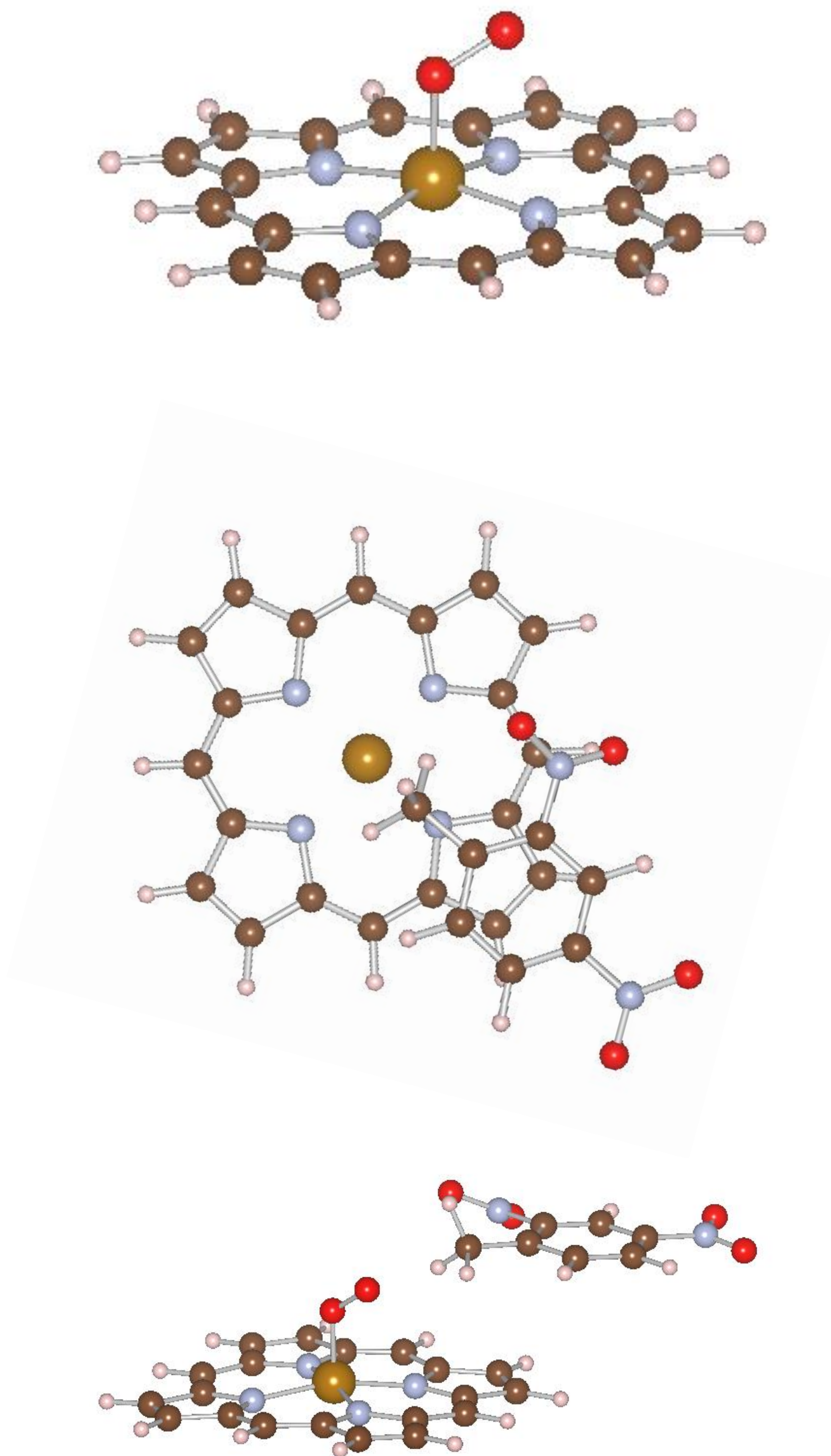

Figure 3.4: Top: profile of O_2 bound to the Fe center of Fe-porphyrin. Center: configuration of the adsorbed DNT on Fe-porphyrin. Bottom: simultaneous adsorption of O_2 and DNT.

Two oxidation reactions are required to complete a full cycle returning the Fe-porphyrin catalyst to its original state. The first DNT oxidation reaction is the same as the "somersault" mechanism for the hydroxylation of hydrocarbons by cytochrome P450, which contains Fe-porphyrin, in biological processes[82] and proceeds as shown schematically in Figure 3.5. Progressing from structure 1 to structure 2, an O_2 molecule from the ambient atmosphere binds to the Fe site with a calculated binding energy of 0.68 eV in the open shell singlet ground state, weakening the O-O bond and lengthening it from 1.2 to 1.3 Å, consistent with other published results.[75,88,89] DNT also adsorbs nearby. We found that, when a DNT molecule approaches the O_2-Fe-porphyrin system, it is energetically favorable for the DNT methyl group to face towards the Fe center (structure 2, Figure 3.5).

The reaction proceeds to structure 3 as a hydrogen atom from the DNT methyl group transfers to the terminal oxygen of the O_2 molecule, a process similar to the dehydrogenation of alkanes by alumina.[90] The resulting OOH structure is metastable with an even further elongated O-O bond of 1.4 Å (structure 3, Figure 3.5). In the final step of the reaction, the O-O bond breaks at the transition state length of 1.6 Å as the new OH group transfers back to the DNT methyl group (structure 4 in Figure 3.5).

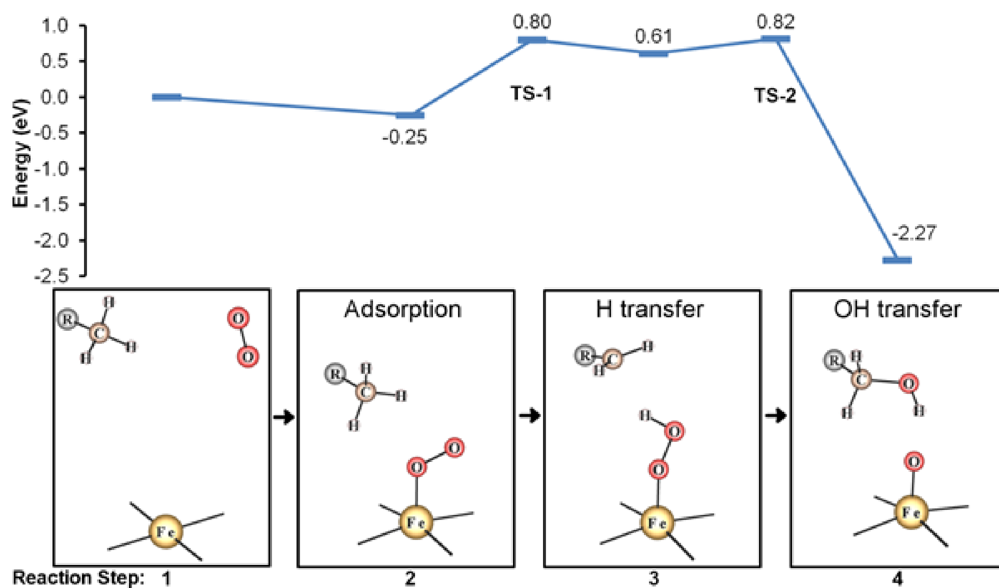

Figure 3.5: Calculated energies of the first reaction with corresponding diagrams of the configuration changes. Dangling bonds indicate the plane of the Fe-porphyrin and R represents the rest of the DNT molecule. The transition state structures are shown in Figure 3.7

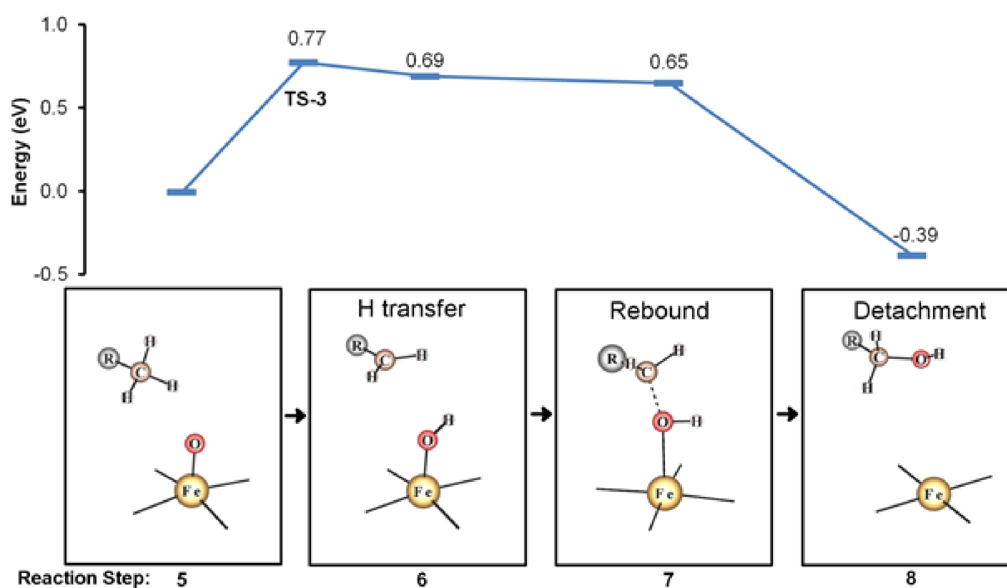

Figure 3.6: Calculated energies of the second reaction with corresponding diagrams of the configuration changes. Dangling bonds indicate the plane of the Fe-porphyrin and R represents the rest of the DNT molecule. Dashed lines indicate a bond that is forming. The transition state structures are shown in Figure 3.7.

The 1 eV (23 kcal mol^{-1}) barrier for this reaction indicates that it can occur at RT. The oxidized DNT product has a 0.4 eV calculated binding energy to the Fe-porphyrin, resulting in a total net release of 1.9 eV after the product desorbs from the Fe-porphyrin.

The completion of the first reaction leaves an atomic oxygen bound to the Fe with a binding energy of 3.8 eV and a Fe-O bond length of 1.6 Å. Thus, it does not desorb by itself, poisoning the catalytic center. To remove the oxygen and restore the catalyst, a self-cleaning reaction similar to the first reaction, depicted in Figure 3.6, can occur. A new DNT molecule approaches the Fe-O site, once more with the methyl group facing the Fe-O site (structure 5, Figure 3.6). The ensuing reaction is the same as the "oxygen rebound" reaction originally proposed for the hydroxylation of hydrocarbons.[82,91,92] As in the first reaction, a hydrogen atom is transferred from the methyl group to the bound oxygen atom (structure 6, Figure 3.6). In the next step, the DNT carbon atom with the dangling bond grabs the OH group (structure 7, Figure 3.6) and resets the molecule to its initial condition (structure 8, Figure 3.6). This step is barrierless. The whole reaction has a barrier of 0.8 eV and a net release of 0.4 eV. We also investigated a reaction pathway for the OH transfer step based on the same somersault mechanism as the initial reaction but found that the barrier is over 2 eV, rendering the reaction pathway infeasible at RT. Similarly, accomplishing the initial reaction by the rebound mechanism instead of the somersault mechanism was found to have an energy barrier of over 1.5 eV, making that pathway infeasible at RT. The transition states associated with the RT-feasible activation barriers in the initial and self-cleaning reactions are depicted in Figure 3.7.

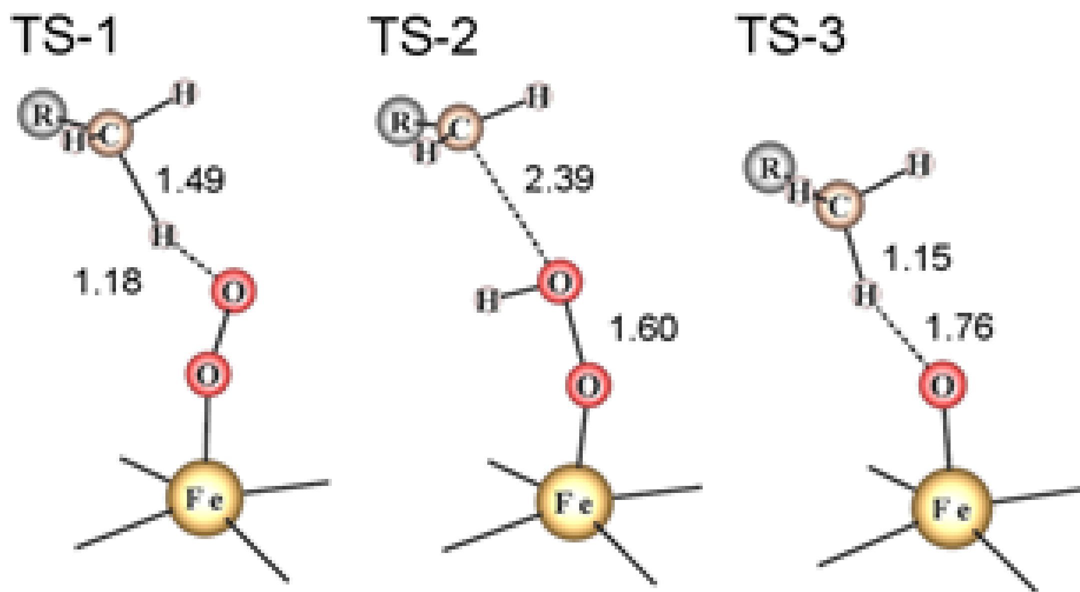

Figure 3.7: Transition state configurations. Dashed lines indicate a bond that is forming. Relevant bond lengths are shown in Å

The rate determining step in the two-reaction process is the H-transfer step in the first reaction. Therefore, we investigated other choices of metalloporphyrin with a different central metal atom to look for evidence of possible further barrier lowering. The binding energies of O_2 and atomic oxygen on Mn-, Fe-, and Co-porphyrin are shown in Figure 3.8. As the O_2 binding energy is fairly constant for these metalloporphyrins, we would not expect a large difference in H-transfer reaction barrier for the first reaction. Although the reaction barrier of the second may vary due to the varying binding energy of atomic oxygen on these metalloporphyrins, it is not the rate-limiting step in the case of Fe-porphyrin.

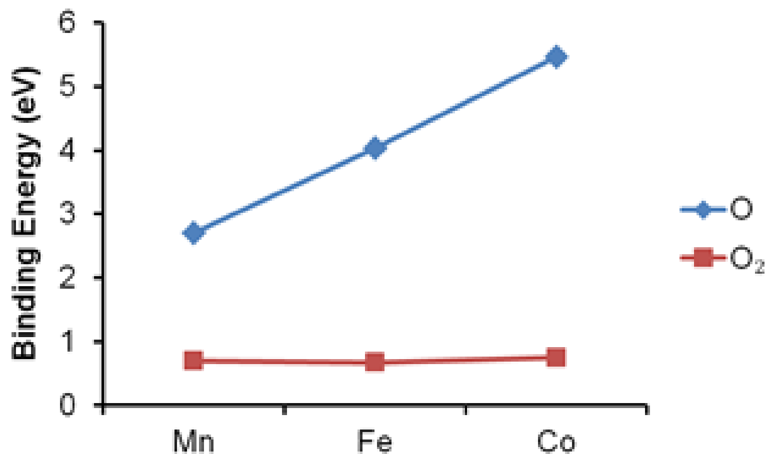

Figure 3.8: Calculated binding energies of O_2 and O on Mn-porphyrin, Fe-porphyrin, and Co-porphyrin.

The following calculation shows how many reactions would be required in a prototype system to cause a significant temperature increase. For a substrate nanostructure with a given volume V, density ρ and specific heat c, the energy E required to cause a $\Delta T = 2$ K rise in temperature is given by

$$E = \Delta T \cdot c \cdot \rho \cdot V \tag{3.1}$$

A possible substrate for the Fe-porphyrin molecule is VO_2, which undergoes a phase transition at 68°C that can be detected optically and can be adjusted to occur at lower temperatures by methods such as doping.[58,93–95] For a VO_2 island with a surface area of 100 nm^2 and thickness of 20 nm corresponding to ρ = 4.6 g/cm^3, V = 2×10^6 nm^3 and specific heat value[96] for VO_2 of c = 0.66 J g^{-1} K^{-1}, we estimate that with 2 eV released per reaction, a density of one reaction for every 2.5 nm^2 of substrate surface area is sufficient to increase the temperature by 2 K. For a functional sensor, the VO_2 islands would have to be on an insulating substrate and their temperature would need to be controlled to within 1 degree. Air containing target molecules might also need to pass through a heating stage.

As described so far, the detection of DNT molecules proceeds “on the fly”, without the DNT molecule adsorbing on the sensor. One can envision adding other molecules on the substrate that might bind the DNT molecule in proximity with the Fe-porphyrin to enhance the sensitivity of the detector and possibly introduce selectivity. Such molecules include peptides with specific binding for DNT.[97]

In summary, we have described first-principles calculations of a reaction wherein Fe-porphyrin enables 2,4-dinitrotoluene (DNT) to react with atmospheric oxygen. The catalyst self-cleans at room temperature by enabling the reaction of another DNT molecule with the remaining atomic oxygen. The heat released by these reactions can in principle be exploited for molecular sensing by joining the catalyst to a substrate with temperature-sensitive optoelectronic properties. Because the reactions are confined to the methyl group, analogous reactions are likely to exist for other toluene compounds.

CHAPTER IV

HYDROGEN DYNAMICS AND METALLIC PHASE STABILIZATION IN VO_2

4.1 VO_2 phase transition properties and device applications

VO_2 is a material of special interest in condensed matter physics due in large part to its unusual electronic phase transition at approximately 68 °C accompanied by a structural phase transition from monoclinic to rutile.[98–101] The unique interplay between thermal, optical, and electronic phenomena in VO_2 makes it a promising material for various applications including optoelectronic switching, solar energy transmittance modulation, nanoscale temperature sensing, and battery cathodes.[102–106]

Various studies have been published investigating the crystallographic and electronic transitions in bulk VO_2, thin VO_2 layers on substrates, and in VO_2 nanoparticles and nanostructures.[58,94,100,107,108] There is significant evidence that doping, strain and defects can all influence the phase transition temperature.[95,109,110] Several dopants such as tungsten and chromium have been used for this purpose, and it has been shown that the dopants affect both electronic and structural properties.[93,110–113] Recent experimental studies supported by total-energy calculations report that heavy hydrogen doping of VO_2 stabilizes the metallic phase at room temperature.[114–116] Engineering of the properties of VO_2 can be improved through a more detailed mechanical understanding of the influence of atomic hydrogen on the VO_2 crystal lattice structure, its dynamics under thermal forcing, and the dissociation and recombination of molecular hydrogen at VO_2 surfaces.

In this chapter we report density functional calculation results that show that the low-temperature metallic phase observed in H-doped VO_2 is due to lattice distortion produced

by interstitial hydrogen atoms binding to oxygen in the lattice, and that the lattice distortion itself is sufficient to produce this metallic phase in undoped VO_2. We also demonstrate the dynamics of hydrogen at the VO_2 surface and in the bulk. Through DFT calculations and first-principles molecular dynamics simulations we find that hydrogen diffuses anisotropically at room temperature along oxygen "channels" in the VO_2 lattice. A surface orientation such as (100) that exposes these channels should more effectively absorb hydrogen than surface orientations where the channels run parallel to the surface. We show that the dissociation of hydrogen molecules at a VO_2 surface into interstitial dopant atoms is energetically favored. We find a 1.6 eV activation barrier for a H_2 molecule dissociation reaction on a (100) surface resulting in atomic hydrogen interstitials and a 1.8 eV activation barrier for the reverse process, suggesting that activation requires elevated temperatures.

4.2 Choice of tools for modeling and calculation

We used density functional theory as implemented in the VASP code with a plane-wave basis to perform binding energy and reaction pathway calculations.[5] Calculations were performed using the generalized gradient approximation with the Hubbard U correction for on-site Coulomb interaction (GGA+U) with U = 4 eV and J = 0.68 eV for Hund's exchange interaction.[117–119] The Perdew, Burke and Ernzerhof (PBE) functional was used for exchange and correlation.[6,7] The method of projector augmented wave (PAW) potentials was used with a cutoff of 400 eV.[87] Bulk VO_2 was represented by a 12-atom supercell (excluding hydrogen), and surface calculations were performed on a freestanding tiled slab produced by a 144-atom supercell (excluding hydrogen) with dimensions of approximately 9.1×10.8×30 Å, leaving a sufficient buffer between slab

layers to isolate them. A 3×3×1 array of k-points including the Γ point was used for Brillouin zone integrations for the surface calculations, and a 7×7×7 array was used for bulk calculations. Reaction paths were calculated with the Climbing Nudged Elastic Band method.[12] All stationary states were converged until all atomic forces were less than 0.05 eV/Å. Hydrogen behavior in VO_2 at finite temperature was simulated with ab-initio molecular dynamics as implemented in VASP. In this case a rutile phase VO_2 supercell of 96 atoms (excluding hydrogen) with dimensions 9.3×9.3×11.2 Å was set to 1000 K as regulated through velocity scaling.

4.3 Phase stabilization and diffusive hydrogen transport

Figure 4.1 depicts the deformation of the monoclinic VO_2 lattice doped with one H for every four V atoms, as compared with the metallic rutile phase of VO_2. The V-V separation in monoclinic VO_2 normally alternates between short and long pair separations, but the hydrogen doping shifts this towards the uniform separation characteristic of the rutile phase, eliminating approximately one third of the difference in short and long V-V separation lengths. This represents a significant portion of a crystallographic transition from the monoclinic to the rutile phase being caused and stabilized by the influence of the hydrogen atoms bonded to the oxygen. Because all chains of V-V separations still exhibit pairing, this distorted monoclinic structure is distinct from the M2 phase observed in some cases of strained or doped VO_2 that has been suggested as a possible intermediate between the monoclinic and rutile phases.[110,120–124]

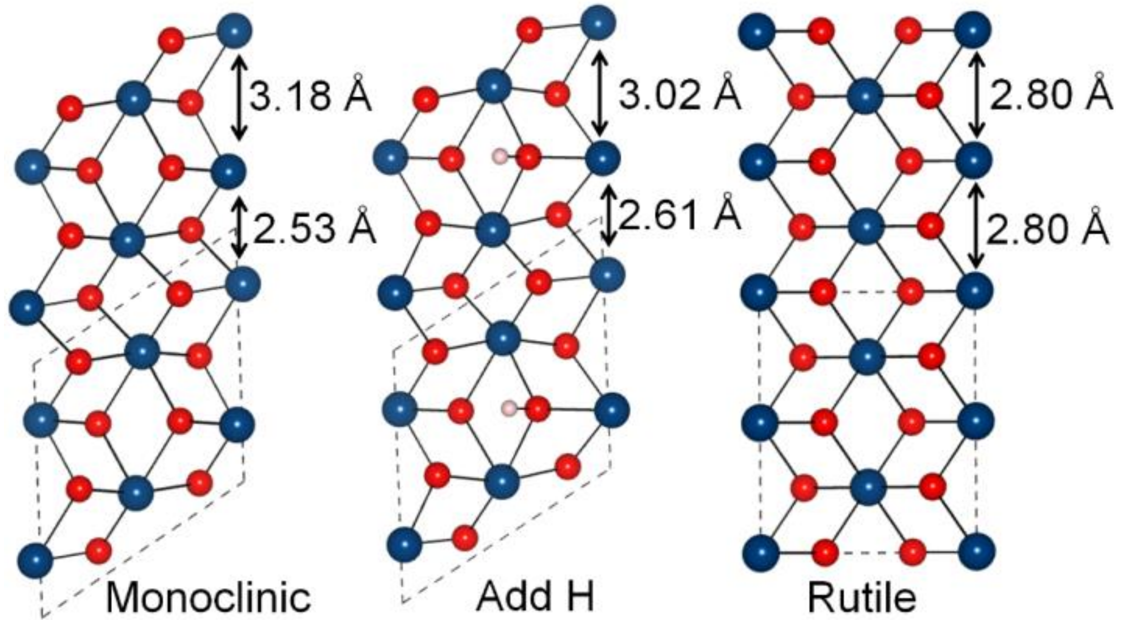

Figure 4.1: Structural deformation of monoclinic VO_2 due to hydrogen doping compared to monoclinic and rutile VO_2.

Figure 4.2 shows the density of states in monoclinic VO_2 and hydrogen-doped VO_2 at energies near the Fermi energy in the material. The calculated band gap for bulk monoclinic VO_2 agrees well with the experimental value of approximately 0.6 eV, especially in light of the well-known tendency of DFT models to underestimate bulk semiconductor band gaps.[125–127] By comparison the hydrogen-doped VO_2 has no band gap at all, and is fully metallic. A rutile structure with an equal doping level of one H for every four V atoms is also metallic, in agreement with prior calculations.[114]

To demonstrate that this band gap filling is caused by the lattice deformation resulting from the hydrogen atoms bonded to the oxygen, and not due to any additional carriers or defect states they might create, a structure was created that is identical to the hydrogen-doped VO_2 but with the hydrogen atoms removed, leaving all other atoms fixed in place. Figure 4.3 shows the density of states for this material near its Fermi energy compared

with the original doped VO_2, and they are qualitatively and quantitatively equivalent. The bulk VO_2 is made metallic purely under the influence of the distorted lattice and atomic arrangement as compared to relaxed monoclinic VO_2.

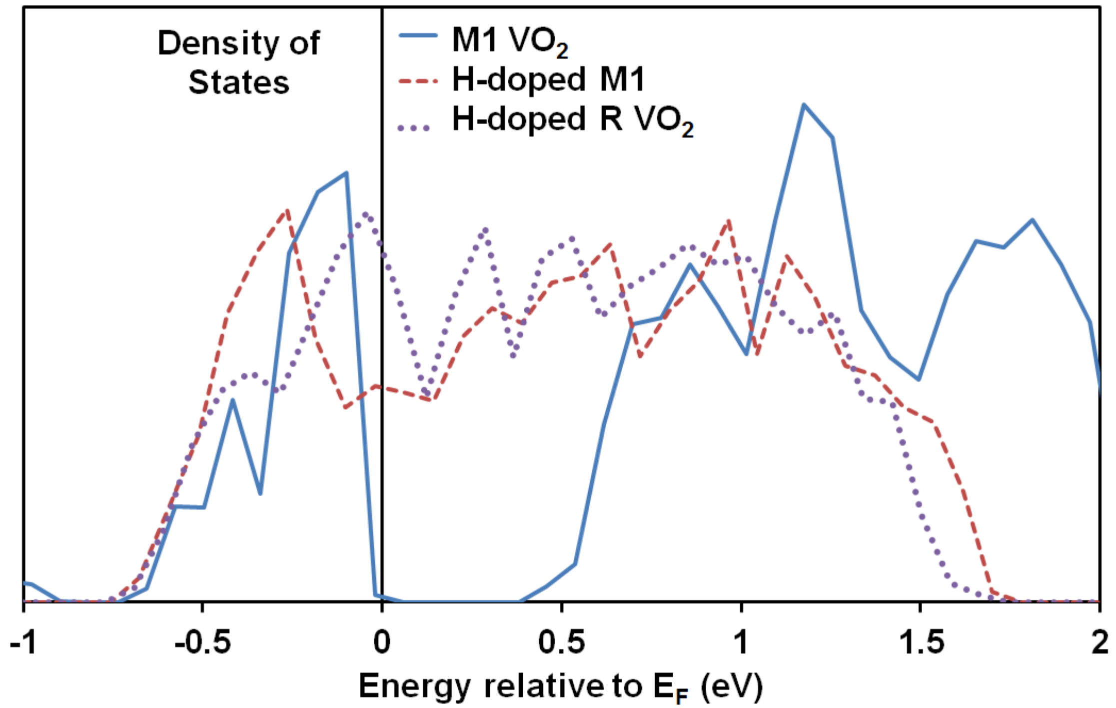

Figure 4.2: Doping the monoclinic (M1) phase of VO_2 with one H for every four V atoms fills the band gap and produces a metallic state, similar to the rutile (R) phase. Removing the hydrogen from doped M1 VO_2 while fixing the other atoms still produces a metallic state through deformation alone.

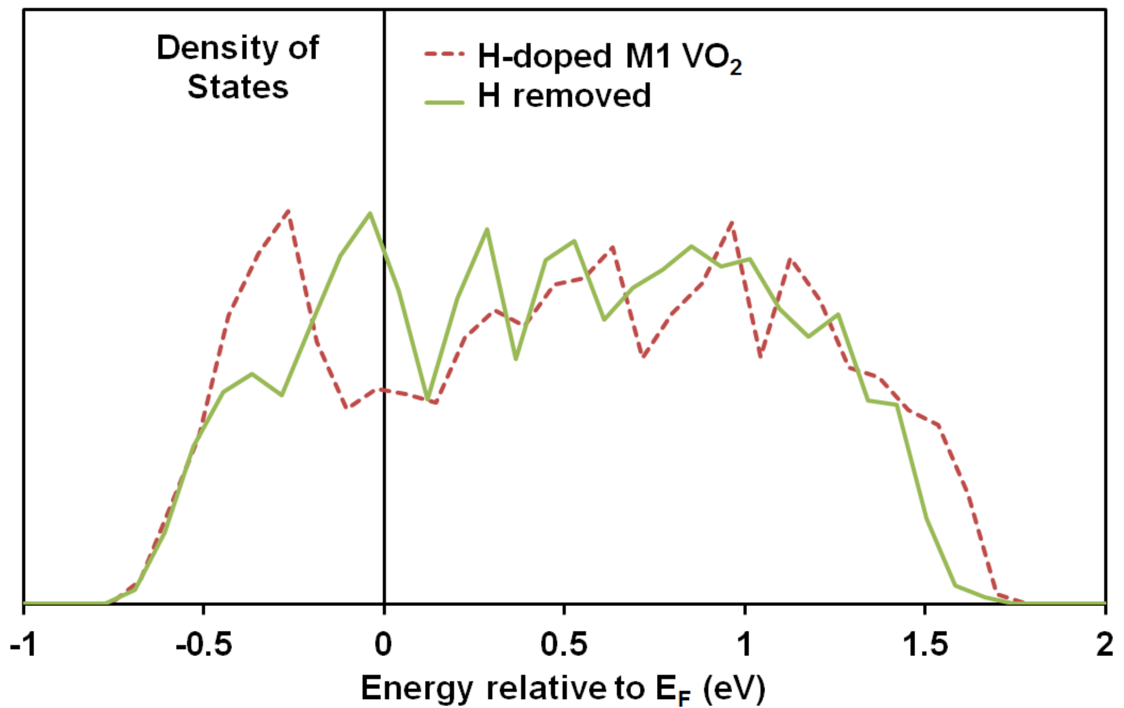

Figure 4.3: Comparison of the density of states near the Fermi energy for H-doped monoclinic VO_2 and for the same fixed structure with all H atoms removed. Removing the hydrogen from doped M1 VO_2 while fixing the other atoms still produces a metallic state through deformation alone.

The dynamics of the interstitial hydrogen atoms in VO_2 under thermal forcing were investigated through a first-principles molecular dynamics simulation. The simulation was performed at 1000 K, and the rutile structure was used for the simulation. The hydrogen atoms are observed to transition between neighboring oxygen atoms with a distinct preference for travel along the [001] direction of the rutile phase (corresponding to the [100] direction of the monoclinic phase), as depicted in Figure 4.4. This figure shows the oxygen channels along which the hydrogen atoms preferentially travel. The preferred binding orientation of the hydrogen to the oxygen makes movements into and out of the figure far easier both kinetically and energetically than switching to the opposite site of the currently bound oxygen. This anisotropy suggests that surfaces that expose the ends of these oxygen channels will more easily absorb and transport atomic hydrogen into the bulk material. Similarly, the same surface should allow easier elimination of the hydrogen atoms to reverse the doping process.

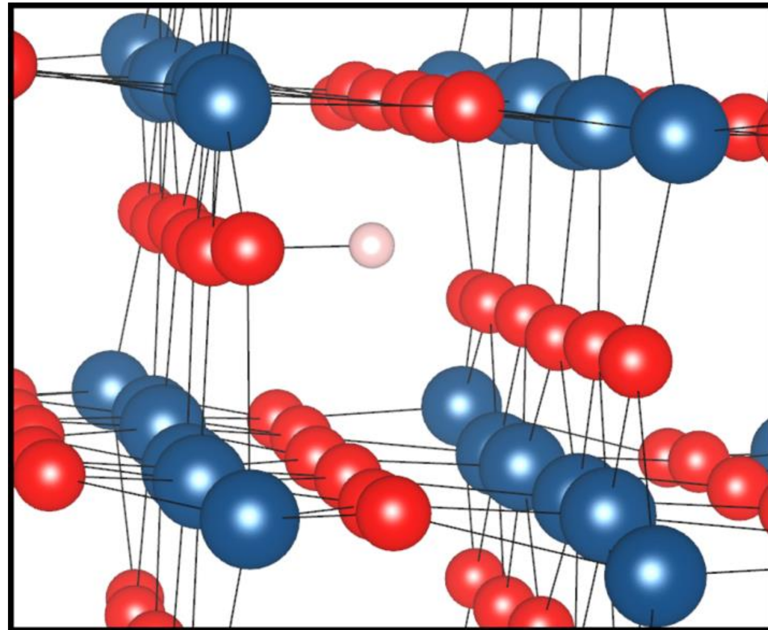

Figure 4.4: A hydrogen interstitial bound to an oxygen in VO_2. Diffusion occurs primarily within the channel going into the figure.

Direct DFT calculations of the energy barriers required for atomic hydrogen to hop from oxygen to oxygen both within and along the channel were performed using the nudged elastic band method. The activation barriers for both atomic migration processes were found to be approximately 0.4 eV. This is easily activated at room temperature, suggesting that interstitial hydrogen is free to reach a fairly homogenous density distribution within bulk VO_2 without high temperature annealing. The calculated binding energy of interstitial atomic hydrogen in VO_2 as compared to molecular hydrogen in vacuum is 0.1 eV per hydrogen, suggesting that hydrogen concentrations at dynamic equilibrium will favor doping more highly than removal from the bulk.

4.4 Implications for tuning of VO_2 properties and controlled hydrogen doping

Atomic hydrogen is shown to be mobile at room temperature in VO_2, but hydrogen primarily occurs naturally as H_2. A direct mechanism for supplying atomic hydrogen to the VO_2 surface through hydrogen dissociation at terminal oxygen ligands was investigated. A nudged elastic band calculation was performed of a hydrogen molecule approaching a VO_2 (100) surface between two exposed oxygen atoms and then splitting to bind each to their nearest oxygen, as depicted in Figure 4.5. This process was calculated to have a barrier of 1.6 eV, consisting of an energetic cost of approximately 0.7 eV for the close approach of the H_2 to the surface and an additional 0.9 eV for the dissociation of the molecule. This barrier is too high for feasible activation without elevated temperatures, and does not provide a competitive alternative to reported doping methods involving aqueous solutions and catalytic spillover.[114,115] Despite the activation barrier, hydrogen dissociation on a VO_2 surface in this manner is found to be energetically favored, resulting in a binding energy of approximately 0.1 eV per

hydrogen as compared to molecular hydrogen in vaccum. This agrees well with the calculated binding energy of atomic hydrogen in bulk VO_2, suggesting that there is little difference in the atomic hydrogen dynamics near the surface and in the bulk. The rather large dissocation barrier and lack of a binding energy for an H_2 molecule on the VO_2 surface suggests that the surface reaction is the rate-determining step for the hydrogen doping process unless an alternative means of supplying atomic hydrogen to the VO_2 surface is utilized. Similarly, the reversible reaction, i.e. recombination of hydrogen to remove the impurities from the bulk, determines the reaction kinetics for the hydrogen elimination process. This reverse process carries an activation barrier of 1.8 eV and a net energy cost of 0.2 eV, suggesting a requirement of elevated temperatures, in agreement with experimental reports of successfully reversing VO_2 hydrogenation by baking at temperatures in excess of 250 °C.[114]

In conclusion, the anisotropic diffusion of hydrogen in VO_2 suggests that certain surface orientations will absorb atomic hydrogen into the bulk more readily than others. These dopant atoms can diffusive readily at room temperature, with a preference for the [100] crystal direction along the oxygen "channels". The interstitial atomic hydrogen bound to oxygen atoms in VO_2 then drives the lattice slightly towards the rutile configuration, and a metallic state is achieved even without completing a crystallographic phase transition. These results suggest hydrogen doping as another method for tuning the critical temperature at which bulk VO_2 becomes metallic. At the high concentrations studied in this chapter the metallic state is present in the ground. More moderate doping is likely to lower this transition temperature. The evidence supporting the ability of a VO_2 surface to dissociate and absorb molecular hydrogen at moderately elevated temperature

may help to optimize the hydrogen assisted phase transition of VO_2 in a more controllable manner by engineering the nanocrystal surface orientation.

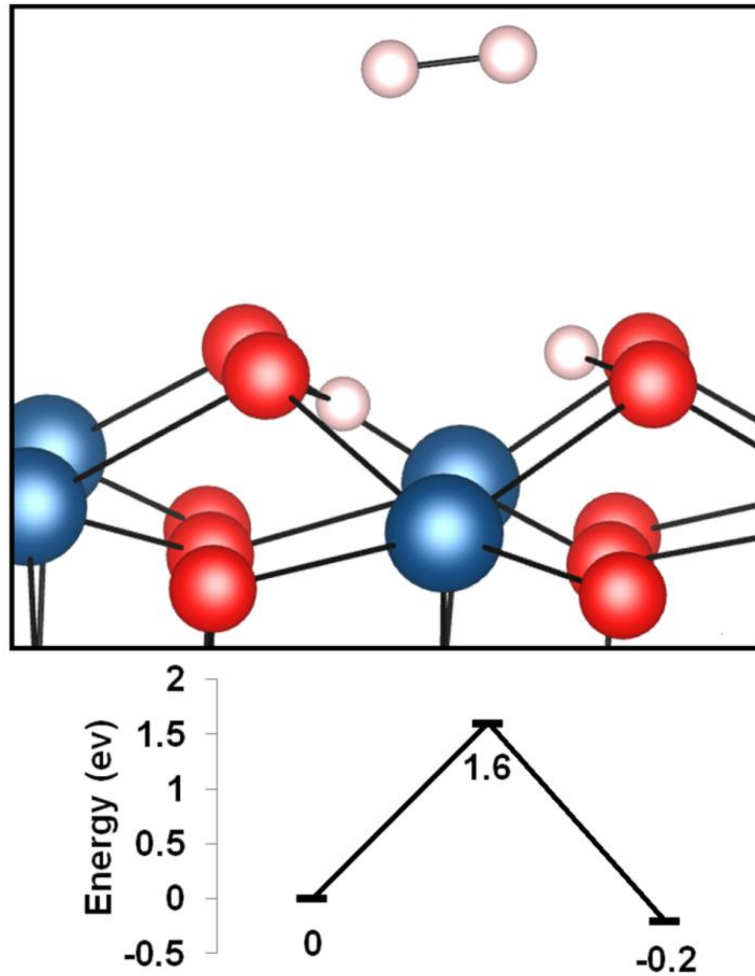

Figure 4.5: A hydrogen molecule begins separated from the VO_2 (100) surface, then approaches the surface and splits towards adjacent oxygens with a 1.6 eV activation barrier, incorporating two atomic hydrogens into the VO_2 with a 0.2 eV net energy release. Initial and final hydrogen states are shown.

APPENDIX A

LIST OF REFEREED JOURNAL ARTICLES

A.1 Work done as part of this thesis

K. H. Warnick, B. Wang, D. E. Cliffel, D. W. Wright, R. F. Haglund, and S. T. Pantelides, "Room-Temperature Reactions for Self-Cleaning Molecular Nanosensors", Nano Lett., 13 (2), pp 798-802 (2013).

K. H. Warnick, Y. Puzyrev, T. Roy, D. M. Fleetwood, R. D. Schrimpf, and S. T. Pantelides, "Room-temperature diffusive phenomena in semiconductors: The case of AlGaN", Phys. Rev. B., 84, 214109 (2011).

A.2 Work done as an undergraduate

T. E. Doyle, A. T. Tew, K. H. Warnick. and B. L. Carruth, "Simulation of elastic wave scattering in cells and tissues at the microscopic level", J. Acoust. Soc. Am. Volume 125, Issue 3, pp. 1751-1767 (2009).

T. E. Doyle, D. A. Robinson, S. B. Jones, K. H. Warnick, and B. L. Carruth, "Modeling the permittivity of two-phase media containing monodisperse spheres: Effects of microstructure and multiple scattering", Physical Review B 76 (5), 054203 (2007).

T. E. Doyle, K. H. Warnick, and B. L. Carruth, "Histology-based simulations for the ultrasonic detection of microscopic cancer in vivo," Journal of the Acoustical Society of America 122 (6), pp EL210-EL216 (2007).

T. E. Doyle, K. H. Warnick, and B. L. Carruth, "Histology-based simulation of ultrasonic scattering in cells and tissues", Journal of the Acoustical Society of America 121 (5), pp. 3111-3111 (2007).

APPENDIX B

LIST OF TALKS AND POSTERS AT INTERNATIONAL MEETINGS

B.1 Talks done as part of this thesis

K. H. Warnick, B. Wang, D. E. Cliffel, D. W. Wright, R. F. Haglund, and Sokrates T. Pantelides, “Room-temperature self-cleaning molecular sensing by catalytic reactions”, BAPS.2013.MAR.Z43.1 in APS March Meeting 2013, Baltimore, Maryland (2013).

K. H. Warnick, Y. Puzyrev, T. Roy, D. M. Fleetwood, R. D. Schrimpf, and S. T. Pantelides, “Field-enhanced vacancy diffusion in AlGaN”, BAPS.2012.MAR.B28.4 in APS March Meeting 2012, Boston, Massachusetts (2012).

K. H. Warnick, B. Wang, and S. T. Pantelides, “Catalytic Reactions of DNT and TNT Molecules on Porphyrin Complexes”, BAPS.2011.MAR.Q10.1 in APS March Meeting 2011, Dallas, Texas (2011).

K. H. Warnick, Y. Puzyrev, T.Roy, D. M. Fleetwood, R. D. Schrimpf, and S. T. Pantelides, "Room-temperature native defect diffusion in semiconductors," EM-WeA9 in AVS 58th International Symposium and Exhibition, Nashville, Tennessee (2011).

K. H. Warnick, Y. Puzyrev, and S. T. Pantelides, “Stress-assisted migration of vacancies in GaN HEMTs”, BAPS.2010.MAR.D25.5 in APS March Meeting 2010, Portland, Oregon (2010).

B.2 Talks done as an undergraduate

C. R. Tolle, K. H. Warnick, John W. James, “Exploration and Development of a new Automated Nonlinear Differential Equation-Based System Identification”, IEEE Eastern Idaho Section meeting (2007). Substituting for Dr. Charles. R. Tolle.

T. E. Doyle, D. A. Robinson, S. B. Jones, and K. H. Warnick, “Modeling the Dielectric Properties of Granular Media to Determine Water Content”, Water Initiative Spring Runoff Conference, Utah State University (2006). Presentation made by T. E. Doyle.

B.3 Posters done as part of this thesis

K. H. Warnick, B. Wang, D. E. Cliffel, D. W. Wright, R. F. Haglund, and S. T. Pantelides, "Catalytic reactions of DNT/TNT molecules on porphyrin complexes," W05-019 in 2011 Chemical and Biological Defense Science and Technology (CBD S&T) Conference, Las Vegas, Nevada (2011).

B.4 Posters done as an undergraduate

K. H. Warnick et. al., “Exploration of Phase Space Reconstruction of Nonlinear Differential Equations using Perona’s Method”, Society for Industrial and Applied Mathematics conference on Applications of Dynamical Systems (2006).

K. H. Warnick et. al., “Reconstructing Systems of Nonlinear Differential Equations from Time Series”, Four Corners Section Fall Meeting of the APS (2006).

K. H. Warnick et. al., “The Galerkin Spectral Method for Modeling Temperature Variations in an Insonified Gas Bubble”, Student Showcase, Utah State University (2007).

K. H. Warnick et. al., “Multipole-based Computer Models of Cellular Acoustic Properties for Ultrasonic Diagnosis”, Student Showcase, Utah State University (2006).

REFERENCES

1. Schrödinger, E. An Undulatory Theory of the Mechanics of Atoms and Molecules. *Phys. Rev.* **28,** 1049–1070 (1926).

2. Hohenberg, P. & Kohn, W. Inhomogeneous Electron Gas. *Phys. Rev.* **136,** B864–B871 (1964).

3. Kohn, W. & Sham, L. J. Self-Consistent Equations Including Exchange and Correlation Effects. *Phys. Rev.* **140,** A1133–A1138 (1965).

4. Perdew, J. P. & Wang, Y. Accurate and simple analytic representation of the electron-gas correlation energy. *Phys. Rev. B* **45,** 13244–13249 (1992).

5. Kresse, G. & Furthmüller, J. Efficient iterative schemes for ab initio total-energy calculations using a plane-wave basis set. *Phys. Rev. B* **54,** 11169–11186 (1996).

6. Perdew, J. P., Burke, K. & Ernzerhof, M. Generalized Gradient Approximation Made Simple. *Phys. Rev. Lett.* **77,** 3865–3868 (1996).

7. Perdew, J. P., Burke, K. & Ernzerhof, M. Generalized Gradient Approximation Made Simple [Phys. Rev. Lett. 77, 3865 (1996)]. *Phys. Rev. Lett.* **78,** 1396–1396 (1997).

8. Perdew, J. P., Ernzerhof, M. & Burke, K. Rationale for mixing exact exchange with density functional approximations. *The Journal of Chemical Physics* **105,** 9982–9985 (1996).

9. Ernzerhof, M. & Scuseria, G. E. Assessment of the Perdew–Burke–Ernzerhof exchange-correlation functional. *The Journal of Chemical Physics* **110,** 5029–5036 (1999).

10. Adamo, C. & Barone, V. Toward reliable density functional methods without adjustable parameters: The PBE0 model. *The Journal of Chemical Physics* **110,** 6158–6170 (1999).

11. Runge, E. & Gross, E. K. U. Density-Functional Theory for Time-Dependent Systems. *Phys. Rev. Lett.* **52,** 997–1000 (1984).

12. Henkelman, G., Uberuaga, B. P. & Jónsson, H. A climbing image nudged elastic band method for finding saddle points and minimum energy paths. *The Journal of Chemical Physics* **113,** 9901–9904 (2000).

13. Henkelman, G. & Jónsson, H. Improved tangent estimate in the nudged elastic band method for finding minimum energy paths and saddle points. *The Journal of Chemical Physics* **113,** 9978–9985 (2000).

14. Chen, K.-C., Wu, W.-W., Liao, C.-N., Chen, L.-J. & Tu, K. N. Observation of Atomic Diffusion at Twin-Modified Grain Boundaries in Copper. *Science* **321,** 1066–1069 (2008).

15. Dekker, J. P., Volkert, C. A., Arzt, E. & Gumbsch, P. Alloying Effects on Electromigration Mass Transport. *Phys. Rev. Lett.* **87,** 035901 (2001).

16. Langdon, T. G. Identifiying creep mechanisms at low stresses. *Materials Science and Engineering: A* **283,** 266–273 (2000).

17. Laks, D. B., Maroudas, D. & Pantelides, S. T. in *Mechanisms in Thin Film Evolution* 449–454 (1994).

18. Gösele, U. M. in *Festkörperprobleme 26* (Grosse, P.) 89–112 (Springer Berlin Heidelberg, 1986). at <http://link.springer.com/chapter/10.1007/BFb0107793>

19. Fahey, P. M., Griffin, P. B. & Plummer, J. D. Point defects and dopant diffusion in silicon. *Rev. Mod. Phys.* **61,** 289–384 (1989).

20. Kandel, D. & Kaxiras, E. Microscopic Theory of Electromigration on Semiconductor Surfaces. *Phys. Rev. Lett.* **76,** 1114–1117 (1996).

21. Van de Walle, C. G. & Neugebauer, J. First-principles calculations for defects and impurities: Applications to III-nitrides. *Journal of Applied Physics* **95,** 3851–3879 (2004).

22. Ganchenkova, M. G. & Nieminen, R. M. Nitrogen Vacancies as Major Point Defects in Gallium Nitride. *Phys. Rev. Lett.* **96,** 196402 (2006).

23. Limpijumnong, S. & Van de Walle, C. G. Diffusivity of native defects in GaN. *Phys. Rev. B* **69,** 035207 (2004).

24. Wright, A. F. Interaction of hydrogen with gallium vacancies in wurtzite GaN. *Journal of Applied Physics* **90,** 1164–1169 (2001).

25. Joh, J. & del Alamo, J. A. Critical Voltage for Electrical Degradation of GaN High-Electron Mobility Transistors. *IEEE Electron Device Letters* **29,** 287–289 (2008).

26. Chowdhury, U. *et al.* TEM Observation of Crack- and Pit-Shaped Defects in Electrically Degraded GaN HEMTs. *IEEE Electron Device Letters* **29,** 1098–1100 (2008).

27. Park, S. Y. *et al.* Physical degradation of GaN HEMT devices under high drain bias reliability testing. *Microelectronics Reliability* **49,** 478–483 (2009).

28. Park, Seong Yong, Lee, Tae Hun & Kim, Moon J. Correlation between Physical Defects and Performance in AlGaN/GaN High Electron Mobility Transistor Devices. *IEEE Trans. Electr. Electron. Mater.* **11,** 49–53 (2010).

29. Del Alamo, J. A. & Joh, J. GaN HEMT reliability. *Microelectronics Reliability* **49,** 1200–1206 (2009).

30. Makaram, P., Joh, J., del Alamo, J. A., Palacios, T. & Thompson, C. V. Evolution of structural defects associated with electrical degradation in AlGaN/GaN high electron mobility transistors. *Applied Physics Letters* **96,** 233509–233509–3 (2010).

31. Joh, J. & del Alamo, J. A. Impact of electrical degradation on trapping characteristics of GaN high electron mobility transistors. in *Electron Devices Meeting, 2008. IEDM 2008. IEEE International* 1–4 (2008). doi:10.1109/IEDM.2008.4796725

32. Sahonta, S.-L., Baines, M. q., Cherns, D., Amano, H. & Ponce, F. a. Migration of Dislocations in Strained GaN Heteroepitaxial Layers. *physica status solidi (b)* **234,** 952–955 (2002).

33. Sugiura, L. Comparison of degradation caused by dislocation motion in compound semiconductor light-emitting devices. *Applied Physics Letters* **70,** 1317–1319 (1997).

34. Janotti, A. & Van de Walle, C. G. Native point defects in ZnO. *Phys. Rev. B* **76,** 165202 (2007).

35. Iddir, H., Öğüt, S., Zapol, P. & Browning, N. Diffusion mechanisms of native point defects in rutile TiO2: Ab initio total-energy calculations. *Phys. Rev. B* **75,** (2007).

36. Capron, N., Broqvist, P. & Pasquarello, A. Migration of oxygen vacancy in HfO2 and across the HfO2⁄SiO2 interface: A first-principles investigation. *Applied Physics Letters* **91,** 192905 (2007).

37. Pennycook, T. J. *et al.* Origin of Colossal Ionic Conductivity in Oxide Multilayers: Interface Induced Sublattice Disorder. *Phys. Rev. Lett.* **104,** 115901 (2010).

38. Vanderbilt, D. Soft self-consistent pseudopotentials in a generalized eigenvalue formalism. *Phys. Rev. B* **41,** 7892–7895 (1990).

39. Floro, J. A., Follstaedt, D. M., Provencio, P., Hearne, S. J. & Lee, S. R. Misfit dislocation formation in the AlGaN/GaN heterointerface. *Journal of Applied Physics* **96,** 7087–7094 (2004).

40. Lee, S. R. *et al.* In situ measurements of the critical thickness for strain relaxation in AlGaN∕GaN heterostructures. *Applied Physics Letters* **85,** 6164–6166 (2004).

41. Somerville, M. H. & del Alamo, J. A. A model for tunneling-limited breakdown in high-power HEMTs. in *Electron Devices Meeting, 1996. IEDM '96., International* 35–38 (1996). doi:10.1109/IEDM.1996.553116

42. Joh, J., Gao, F., Palacios, T. & del Alamo, J. A. A model for the critical voltage for electrical degradation of GaN high electron mobility transistors. *Microelectronics Reliability* **50,** 767–773 (2010).

43. Puzyrev, Y. S. *et al.* Dehydrogenation of defects and hot-electron degradation in GaN high-electron-mobility transistors. *Journal of Applied Physics* **109,** 034501–034501–8 (2011).

44. Laaksonen, K., Ganchenkova, M. G. & Nieminen, R. M. Vacancies in wurtzite GaN and AlN. *J. Phys.: Condens. Matter* **21,** 015803 (2009).

45. Kuo, Y.-K., Lin, W.-W. & Lin, J. Band-Gap Bowing Parameter of the $In_xGa_{1-x}N$ Derived From Theoretical Simulation. *Japanese Journal of Applied Physics* **40,** 3157–3158 (2001).

46. Warnick, K. H. *et al.* Room-temperature diffusive phenomena in semiconductors: The case of AlGaN. *Phys. Rev. B* **84,** 214109 (2011).

47. Devine, R. A. B., Mathiot, D., Warren, W. L., Fleetwood, D. M. & Aspar, B. Point defect generation during high temperature annealing of the Si #x2010;SiO2 interface. *Applied Physics Letters* **63,** 2926–2928 (1993).

48. Baù, L., Tecilla, P. & Mancin, F. Sensing with fluorescent nanoparticles. *Nanoscale* **3,** 121–133 (2011).

49. Che, Y., Yang, X., Loser, S. & Zang, L. Expedient Vapor Probing of Organic Amines Using Fluorescent Nanofibers Fabricated from an n-Type Organic Semiconductor. *Nano Lett.* **8,** 2219–2223 (2008).

50. Naddo, T. *et al.* Detection of Explosives with a Fluorescent Nanofibril Film. *J. Am. Chem. Soc.* **129,** 6978–6979 (2007).

51. Liu, D., Wang, Z. & Jiang, X. Gold nanoparticles for the colorimetric and fluorescent detection of ions and small organic molecules. *Nanoscale* **3,** 1421–1433 (2011).

52. Wang, D. *et al.* Chemiresistive response of silicon nanowires to trace vapor of nitro explosives. *Nanoscale* **4,** 2628–2632 (2012).

53. Gao, C., Guo, Z., Liu, J.-H. & Huang, X.-J. The new age of carbon nanotubes: An updated review of functionalized carbon nanotubes in electrochemical sensors. *Nanoscale* **4,** 1948–1963 (2012).

54. An, Q. *et al.* Silver-coated magnetite–carbon core–shell microspheres as substrate-enhanced SERS probes for detection of trace persistent organic pollutants. *Nanoscale* **4,** 5210–5216 (2012).

55. Sajanlal, P. R. & Pradeep, T. Functional hybrid nickel nanostructures as recyclable SERS substrates: detection of explosives and biowarfare agents. *Nanoscale* **4,** 3427–3437 (2012).

56. Bonnot, K., Siegert, B., Cottineau, T., Keller, V. & Spitzer, D. Design of an efficient measurement cell for characterizing sensing properties of nanostructured sensitive layers coated on chips. *Sensors and Actuators B: Chemical* **166–167,** 829–832 (2012).

57. Chen, D. *et al.* Hierarchically plasmonic photocatalysts of Ag/AgCl nanocrystals coupled with single-crystalline WO3 nanoplates. *Nanoscale* (2012). doi:10.1039/C2NR31030A

58. Lopez, R., Haynes, T. E., Boatner, L. A., Feldman, L. C. & Haglund, J. Temperature-controlled surface plasmon resonance in VO 2 nanorods. *Opt. Lett.* **27,** 1327–1329 (2002).

59. Wang, B., Wright, D., Cliffel, D., Haglund, R. & Pantelides, S. T. Ionization-Enhanced Decomposition of 2,4,6-Trinitrotoluene (TNT) Molecules. *J. Phys. Chem. A* **115,** 8142–8146 (2011).

60. Li, L., Gloyna, E. F. & Sawicki, J. E. Treatability of DNT Process Wastewater by Supercritical Water Oxidation. *Water Environment Research* **65,** 250–257 (1993).

61. Ju, K.-S. & Parales, R. E. Nitroaromatic Compounds, from Synthesis to Biodegradation. *Microbiol. Mol. Biol. Rev.* **74,** 250–272 (2010).

62. Chen, W.-S., Juan, C.-N. & Wei, K.-M. Mineralization of dinitrotoluenes and trinitrotoluene of spent acid in toluene nitration process by Fenton oxidation. *Chemosphere* **60,** 1072–1079 (2005).

63. Venkatadri, R. & Peters, R. W. Chemical Oxidation Technologies: Ultraviolet Light/Hydrogen Peroxide, Fenton's Reagent, and Titanium Dioxide-Assisted Photocatalysis. *Hazardous Waste and Hazardous Materials* **10,** 107–149 (1993).

64. Que, L. & Tolman, W. B. Biologically inspired oxidation catalysis. *Nature* **455,** 333–340 (2008).

65. Suen, W. C., Haigler, B. E. & Spain, J. C. 2,4-Dinitrotoluene dioxygenase from Burkholderia sp. strain DNT: similarity to naphthalene dioxygenase. *J. Bacteriol.* **178,** 4926–4934 (1996).

66. Oh, S.-Y., Kang, S.-G. & Chiu, P. C. Degradation of 2,4-dinitrotoluene by persulfate activated with zero-valent iron. *Science of The Total Environment* **408,** 3464–3468 (2010).

67. Monti, M. R., Smania, A. M., Fabro, G., Alvarez, M. E. & Argaraña, C. E. Engineering Pseudomonas fluorescens for Biodegradation of 2,4-Dinitrotoluene. *Appl. Environ. Microbiol.* **71,** 8864–8872 (2005).

68. Li, Z. M., Shea, P. J. & Comfort, S. D. Nitrotoluene destruction by UV-catalyzed fenton oxidation. *Chemosphere* **36,** 1849–1865 (1998).

69. Liou, M.-J., Lu, M.-C. & Chen, J.-N. Oxidation of explosives by Fenton and photo-Fenton processes. *Water Research* **37,** 3172–3179 (2003).

70. Jiang, R. & Chu, D. Remarkably Active Catalysts for the Electroreduction of O[sub 2] to H[sub 2]O for Use in an Acidic Electrolyte Containing Concentrated Methanol. *J. Electrochem. Soc.* **147,** 4605–4609 (2000).

71. Murahashi, S.-I., Naota, T. & Komiya, N. Metalloporphyrin-Catalyzed Oxidation of Alkanes with Molecular Oxygen in the Presence of Acetaldehyde. *Tetrahedron Letters* **36,** 8059–8062 (1995).

72. Lyons, J. E., Ellis, P. E. & Myers, H. K. Halogenated Metalloporphyrin Complexes as Catalysts for Selective Reactions of Acyclic Alkanes with Molecular Oxygen. *Journal of Catalysis* **155,** 59–73 (1995).

73. Sharma, S., Singh, H., Harvey, J. N. & Balint-Kurti, G. G. Design of an infrared laser pulse to control the multiphoton dissociation of the Fe–CO bond in CO-heme compounds. *The Journal of Chemical Physics* **133,** 174103–174103–11 (2010).

74. Salazar-Salinas, K., Jauregui, L. A., Kubli-Garfias, C. & Seminario, J. M. Molecular biosensor based on a coordinated iron complex. *The Journal of Chemical Physics* **130,** 105101–105101–9 (2009).

75. Liu, H. *et al.* Theoretical investigation on the chemical sensing of metalloporphyrin-based molecular junction. *The Journal of Chemical Physics* **132,** 244702–244702–9 (2010).

76. Van Rantwijk, F. & Sheldon, R. A. Selective oxygen transfer catalysed by heme peroxidases: synthetic and mechanistic aspects. *Current Opinion in Biotechnology* **11,** 554–564 (2000).

77. Berglund, G. I. *et al.* The catalytic pathway of horseradish peroxidase at high resolution. *Nature* **417,** 463–468 (2002).

78. Greenwood, C. & Gibson, Q. H. The Reaction of Reduced Cytochrome c Oxidase with Oxygen. *J. Biol. Chem.* **242,** 1782–1787 (1967).

79. Blair, D. F., Witt, S. N. & Chan, S. I. Mechanism of cytochrome c oxidase-catalyzed dioxygen reduction at low temperatures. Evidence for two intermediates at the three-electron level and entropic promotion of the bond-breaking step. *J. Am. Chem. Soc.* **107,** 7389–7399 (1985).

80. Hofacker, I. & Schulten, K. Oxygen and proton pathways in cytochrome c oxidase. *Proteins* **30,** 100–107 (1998).

81. Fasan, R. Tuning P450 Enzymes as Oxidation Catalysts. *ACS Catal.* **2,** 647–666 (2012).

82. Bach, R. D. & Dmitrenko, O. The 'Somersault' Mechanism for the P-450 Hydroxylation of Hydrocarbons. The Intervention of Transient Inverted Metastable Hydroperoxides. *J. Am. Chem. Soc.* **128,** 1474–1488 (2006).

83. De Visser, S. P. & Shaik, S. A Proton-Shuttle Mechanism Mediated by the Porphyrin in Benzene Hydroxylation by Cytochrome P450 Enzymes. *J. Am. Chem. Soc.* **125,** 7413–7424 (2003).

84. Ji, L.-N., Liu, M., Hsieh, A.-K. & Hor, T. S. A. Metalloporphyrin-catalyzed hydroxylation of cyclohexane with molecular oxygen. *Journal of Molecular Catalysis* **70,** 247–257 (1991).

85. Daniel, M. A brief history of the contribution of metalloporphyrin models to cytochrome P450 chemistry and oxidation catalysis. *Comptes Rendus Chimie* **10,** 392–413 (2007).

86. Shaik, S. *et al.* P450 Enzymes: Their Structure, Reactivity, and Selectivity—Modeled by QM/MM Calculations. *Chem. Rev.* **110,** 949–1017 (2009).

87. Blöchl, P. E. Projector augmented-wave method. *Phys. Rev. B* **50,** 17953–17979 (1994).

88. Sun, Y., Chen, K., Jia, L. & Li, H. Toward understanding macrocycle specificity of iron on the dioxygen-binding ability: a theoretical study. *Phys. Chem. Chem. Phys.* **13,** 13800–13808 (2011).

89. Shi, Z. & Zhang, J. Density Functional Theory Study of Transitional Metal Macrocyclic Complexes' Dioxygen-Binding Abilities and Their Catalytic Activities toward Oxygen Reduction Reaction. *J. Phys. Chem. C* **111,** 7084–7090 (2007).

90. Borisevich, A. Y. *et al.* Dual Nanoparticle/Substrate Control of Catalytic Dehydrogenation. *Advanced Materials* **19,** 2129–2133 (2007).

91. Groves, J. T. & McClusky, G. A. Aliphatic hydroxylation via oxygen rebound. Oxygen transfer catalyzed by iron. *J. Am. Chem. Soc.* **98,** 859–861 (1976).

92. Balcells, D., Raynaud, C., Crabtree, R. H. & Eisenstein, O. The rebound mechanism in catalytic C–H oxidation by MnO(tpp)Cl from DFT studies: electronic nature of the active species. *Chem. Commun.* 744–746 (2008). doi:10.1039/B715939K

93. Tan, X. *et al.* Unraveling Metal-insulator Transition Mechanism of VO2 Triggered by Tungsten Doping. *Sci Rep* **2,** (2012).

94. Lopez, R., Feldman, L. C. & Haglund, R. F. Size-Dependent Optical Properties of VO_{2} Nanoparticle Arrays. *Phys. Rev. Lett.* **93,** 177403 (2004).

95. Lopez, R., Haynes, T. E., Boatner, L. A., Feldman, L. C. & Haglund, R. F. Size effects in the structural phase transition of VO_{2} nanoparticles. *Phys. Rev. B* **65,** 224113 (2002).

96. Berglund, C. N. & Guggenheim, H. J. Electronic Properties of VO_{2} near the Semiconductor-Metal Transition. *Phys. Rev.* **185,** 1022–1033 (1969).

97. Jaworski, J. W., Raorane, D., Huh, J. H., Majumdar, A. & Lee, S.-W. Evolutionary Screening of Biomimetic Coatings for Selective Detection of Explosives. *Langmuir* **24,** 4938–4943 (2008).

98. Morin, F. J. Oxides Which Show a Metal-to-Insulator Transition at the Neel Temperature. *Phys. Rev. Lett.* **3,** 34–36 (1959).

99. Zylbersztejn, A. & Mott, N. F. Metal-insulator transition in vanadium dioxide. *Phys. Rev. B* **11,** 4383–4395 (1975).

100. Sohn, J. I. *et al.* Direct Observation of the Structural Component of the Metal−Insulator Phase Transition and Growth Habits of Epitaxially Grown VO2 Nanowires. *Nano Lett.* **7,** 1570–1574 (2007).

101. Goodenough, J. B. The two components of the crystallographic transition in VO2. *Journal of Solid State Chemistry* **3,** 490–500 (1971).

102. Kasırga, T. S. *et al.* Photoresponse of a strongly correlated material determined by scanning photocurrent microscopy. *Nat Nano* **7,** 723–727 (2012).

103. Chang, S.-J. *et al.* Probing the photothermally induced phase transitions in single-crystalline vanadium dioxide nanobeams. *Nanotechnology* **24,** 345701 (2013).

104. Chen, W., Peng, J., Mai, L., Yu, H. & Qi, Y. Fabrication of Novel Vanadium Dioxide Nanorods as Cathode Material for Rechargeable Lithium Batteries. *Chemistry Letters* **33,** 1366–1367 (2004).

105. Li, S.-Y., Niklasson, G. A. & Granqvist, C. G. Nanothermochromics: Calculations for VO[sub 2] nanoparticles in dielectric hosts show much improved luminous transmittance and solar energy transmittance modulation. *Journal of Applied Physics* **108,** 063525 (2010).

106. Warnick, K. H. *et al.* Room-Temperature Reactions for Self-Cleaning Molecular Nanosensors. *Nano Lett.* **13,** 798–802 (2013).

107. Andreev, V. N., Kapralova, V. M. & Klimov, V. A. Effect of hydrogenation on the metal-semiconductor phase transition in vanadium dioxide thin films. *Phys. Solid State* **49,** 2318–2322 (2007).

108. Haverkort, M. W. *et al.* Orbital-Assisted Metal-Insulator Transition in VO_{2}. *Phys. Rev. Lett.* **95,** 196404 (2005).

109. Cao, J. *et al.* Extended Mapping and Exploration of the Vanadium Dioxide Stress-Temperature Phase Diagram. *Nano Lett.* **10,** 2667–2673 (2010).

110. Pouget, J. P., Launois, H., D'Haenens, J. P., Merenda, P. & Rice, T. M. Electron Localization Induced by Uniaxial Stress in Pure VO_{2}. *Phys. Rev. Lett.* **35,** 873–875 (1975).

111. McWhan, D. B., Marezio, M., Remeika, J. P. & Dernier, P. D. X-ray diffraction study of metallic VO_{2}. *Phys. Rev. B* **10,** 490–495 (1974).

112. Marezio, M., McWhan, D. B., Remeika, J. P. & Dernier, P. D. Structural Aspects of the Metal-Insulator Transitions in Cr-Doped VO_{2}. *Phys. Rev. B* **5,** 2541–2551 (1972).

113. Patridge, C. J., Whittaker, L., Ravel, B. & Banerjee, S. Elucidating the Influence of Local Structure Perturbations on the Metal–Insulator Transitions of V1–xMoxO2 Nanowires: Mechanistic Insights from an X-ray Absorption Spectroscopy Study. *J. Phys. Chem. C* **116,** 3728–3736 (2012).

114. Wei, J., Ji, H., Guo, W., Nevidomskyy, A. H. & Natelson, D. Hydrogen stabilization of metallic vanadium dioxide in single-crystal nanobeams. *Nat Nano* **7,** 357–362 (2012).

115. Hong, W.-K. *et al.* Hydrogen-Induced Morphotropic Phase Transformation of Single-Crystalline Vanadium Dioxide Nanobeams. *Nano Lett.* **13,** 1822–1828 (2013).

116. Wu, C. *et al.* Hydrogen-Incorporation Stabilization of Metallic VO2(R) Phase to Room Temperature, Displaying Promising Low-Temperature Thermoelectric Effect. *J. Am. Chem. Soc.* **133,** 13798–13801 (2011).

117. Anisimov, V. I., Aryasetiawan, F. & Lichtenstein, A. I. First-principles calculations of the electronic structure and spectra of strongly correlated systems: the LDA+ U method. *J. Phys.: Condens. Matter* **9,** 767 (1997).

118. Biermann, S., Poteryaev, A., Lichtenstein, A. I. & Georges, A. Dynamical Singlets and Correlation-Assisted Peierls Transition in VO_{2}. *Phys. Rev. Lett.* **94,** 026404 (2005).

119. Cococcioni, M. & de Gironcoli, S. Linear response approach to the calculation of the effective interaction parameters in the LDA+U method. *Phys. Rev. B* **71,** 035105 (2005).

120. Guo, H. *et al.* Mechanics and Dynamics of the Strain-Induced M1–M2 Structural Phase Transition in Individual VO2 Nanowires. *Nano Lett.* **11,** 3207–3213 (2011).

121. Sohn, J. I. *et al.* Surface-Stress-Induced Mott Transition and Nature of Associated Spatial Phase Transition in Single Crystalline VO2 Nanowires. *Nano Lett.* **9,** 3392–3397 (2009).

122. Pouget, J. P. *et al.* Dimerization of a linear Heisenberg chain in the insulating phases of V_{1-x}Cr_{x}O_{2}. *Phys. Rev. B* **10,** 1801–1815 (1974).

123. Zhang, S., Chou, J. Y. & Lauhon, L. J. Direct Correlation of Structural Domain Formation with the Metal Insulator Transition in a VO2 Nanobeam. *Nano Lett.* **9,** 4527–4532 (2009).

124. Jones, A. C., Berweger, S., Wei, J., Cobden, D. & Raschke, M. B. Nano-optical Investigations of the Metal−Insulator Phase Behavior of Individual VO2 Microcrystals. *Nano Lett.* **10,** 1574–1581 (2010).

125. Perdew, J. P. & Levy, M. Physical Content of the Exact Kohn-Sham Orbital Energies: Band Gaps and Derivative Discontinuities. *Phys. Rev. Lett.* **51,** 1884–1887 (1983).

126. Verleur, H. W., Barker, A. S. & Berglund, C. N. Optical Properties of VO_{2} between 0.25 and 5 eV. *Phys. Rev.* **172,** 788–798 (1968).

127. Qazilbash, M. M. *et al.* Mott Transition in VO2 Revealed by Infrared Spectroscopy and Nano-Imaging. *Science* **318,** 1750–1753 (2007).